

Dated: 20 December 2021

The Virgo Collaboration + additional authors

. To be submitted to CQG

*Virgo INTERNAL DOCUMENT – NOT FOR PUBLIC DISTRIBUTION*

## The Virgo O3 run and the impact of the environment

The Virgo Collaboration + a few additional authors

**Abstract.** Sources of geophysical noise (such as wind, sea waves and earthquakes) or of anthropogenic noise impact ground-based gravitational-wave interferometric detectors, causing transient sensitivity worsening and gaps in data taking. During the one year-long third Observing Run (O3: from April 01, 2019 to March 27, 2020), the Virgo Collaboration collected a statistically significant dataset, used in this article to study the response of the detector to a variety of environmental conditions. We correlated environmental parameters to global detector performance, such as observation range, duty cycle and control losses. Where possible, we identified weaknesses in the detector that will be used to elaborate strategies in order to improve Virgo robustness against external disturbances for the next data taking period, O4, currently planned to start in the second semester of 2022. The lessons learned could also provide useful insights for the design of the next generation of ground-based interferometers.

18 **Contents**

19 **1 Introduction** **3**

20 **2 The Virgo environmental monitoring during O3** **5**

21 **3 Seismic noise** **7**

22 3.1 The seismic frequency bands and their evolution during the O3 run . . . 7

23 3.2 Impact on the Virgo detector . . . . . 11

24 3.2.1 Sensitivity . . . . . 11

25 3.2.2 Duty cycle . . . . . 12

26 **4 Earthquakes** **14**

27 4.1 Seismon and O3 setup at EGO . . . . . 15

28 4.2 Earthquakes impact during O3 . . . . . 16

29 4.3 Plans for O4 . . . . . 22

30 **5 Bad weather** **22**

31 5.1 Impact of sea activity . . . . . 23

32 5.1.1 Microseism impact on strain noise . . . . . 23

33 5.1.2 Microseism impact on glitch rates . . . . . 23

34 5.1.3 Microseism and scattered light . . . . . 24

35 5.1.4 Identification of scattered light culprits . . . . . 27

36 5.2 Impact of wind . . . . . 28

37 5.3 Disentangling sea activity and wind . . . . . 30

38 **6 Other environment impacts** **31**

39 6.1 Magnetic noise . . . . . 31

40 6.2 Lightnings . . . . . 32

41 6.3 Cosmic muons . . . . . 34

42 **7 Outlook and prospects for O4** **36**

43 **Appendix A Study of the lock losses during O3** **38**

## 44 1. Introduction

45 The past decade has seen the ramp-up of the second-generation ('Advanced') earth-based  
46 gravitational-wave (GW) detectors. Design improvements and technological upgrades  
47 have paved the way to the first direct detections of GWs by the global network made up  
48 of the two aLIGO instruments [1] (located in the USA: Hanford, WA and Livingston,  
49 LA) and of the Advanced Virgo detector [2] (located in Cascina, Italy). The main  
50 results achieved by the LIGO Scientific Collaboration and the Virgo Collaboration –  
51 recently joined by the KAGRA collaboration whose detector [3], located under the  
52 Kamioka mountain in Japan, is nearing completion – include the first detection of  
53 a binary black hole merger (GW150914 [4]); the first detection of a binary neutron  
54 star merger (GW170817 [5]) that lead to the birth of multi-messenger astronomy with  
55 GW [6]; and now dozens of detections of compact binary mergers that add up in a GW  
56 Transient Catalogue regularly updated [7, 8]. These detections contribute to opening  
57 a new window onto the Universe by providing insights to the populations of compact  
58 objects and the binary merger rates [9]; they also allow scientists to perform stringent  
59 tests of general relativity [10] in a new regime of gravitation never probed before.

60 The operation of ground-based GW detectors is organized into successive steps forming a  
61 recurring sequence over the years: upgrades; commissioning and sensitivity improvement  
62 (the so-called *noise hunting* phase); data-taking periods called observing runs (or simply  
63 runs and labelled *On*). So far there have been three runs for the global network of  
64 advanced detectors.

- 65 • O1 (09/2015 – 01/2016) with only the two LIGO detectors taking data;
- 66 • O2 (11/2016 – 08/2017) with Virgo joining LIGO on August 01;
- 67 • finally O3 (04/2019 – 03/2020), that saw the three detectors take data jointly  
68 during 11 months in total: 6 months first (called O3a), followed by a 1-month  
69 break (October 2019) and then another period of 5 months of data taking (O3b),  
70 interrupted about a month earlier than expected due to the worldwide COVID-19  
71 pandemic.

72 The above listing shows that the O3 run was the first *long* data-taking period for the  
73 Advanced Virgo detector. Therefore, we have used the wealth of unprecedented data  
74 collected during this year to make an in-depth analysis of the instrument performance.  
75 In this article, we study the impact of the environment on Advanced Virgo, along the  
76 lines of previous publications from Virgo [11], LIGO [12] or KAGRA [13]. We focus on  
77 various types of seismic noises, on earthquakes and on bad weather periods. We also  
78 briefly investigate the effect of other possible disturbances: magnetic noise, lightning  
79 and cosmic muons. Our goal is threefold: to quantify how the Virgo sensitivity and  
80 duty cycle depend on these external parameters; to use this knowledge to prepare the  
81 next run, O4, scheduled to start in the second semester 2022; finally, to build experience  
82 for future GW detectors, in particular for the Einstein Telescope project [14].

83 The Virgo detector is located in Italy at EGO, the European Gravitational Observatory,  
 84 in the municipality of Cascina. The EGO site is in the countryside, about 12 km south-  
 85 east of Pisa and about 17 km east of the Tyrrhenian coast. Virgo is not far from some  
 86 industrial and commercial sites that can generate noise. Within 7 km from EGO there  
 87 are: elevated highways, railway tracks, wind turbines, earth quarries, electroducts and  
 88 the Pisa airport. To avoid pressure waves potentially shaking the ground, a no-fly zone  
 89 has been enforced in a cylindrical volume (600 m radius and height) above each of the  
 90 Virgo experimental buildings.

91 Advanced Virgo is a power-recycled Michelson interferometer with Fabry-Perot cavities  
 92 in its 3 km-long arms. All core optics are suspended to long suspensions, called the  
 93 superattenuators [15], that have a twofold use: first, to isolate as much as possible the  
 94 mirrors from seismic motions (both vertical and longitudinal), and then to control very  
 95 accurately their positions in all six degrees of freedom. Many feedback systems are used  
 96 to bring the detector to its working point and maintain it there [16, 17]. This state – the  
 97 same for O2 and O3: the Michelson interferometer on a dark fringe, the Fabry-Perot and  
 98 power recycling cavities in resonance – is the only one in which the detector is sensitive  
 99 to the passing of GWs.

100 The phase when the interferometer is brought to its working point with feedback loops  
 101 closed is called *lock acquisition* or *locking*. The detector is said to be *locked* when it  
 102 is kept at its working point by its global control system. A *lock loss* occurs when the  
 103 detector cannot be controlled anymore and its working point is lost. The most common  
 104 sequence during data taking is locking → locked → data taking in Science mode → lock  
 105 loss → locking again, etc.

106 During a run, priority is obviously given to taking data of quality good enough to be  
 107 included in physics analysis. Virgo is said to be in *Science mode*. During O3, the average  
 108 duty cycle in Science mode has been around 76% [18], with the remaining time almost  
 109 equally equally into three categories.

- 110 • Locking and adjustment phases, to restore the working point and restart taking  
 111 data in Science mode;
- 112 • Recurring controlled actions on the detector: maintenance (usually a few hours  
 113 on Tuesday mornings local time), calibration (usually every Wednesday evening)  
 114 or commissioning (measurements, working point tuning or tailored improvements:  
 115 sessions organized when the need arises);
- 116 • Problems preventing a smooth running of the detector.

117 The article is organized as follows. Section 2 describes the environmental monitoring  
 118 of the Virgo detector during the O3 run. Section 3 is dedicated to the different seismic  
 119 noise contributions (either natural or human-related): how to disentangle them, how  
 120 to monitor them and what their impacts on the detector are in terms of sensitivity  
 121 and duty cycle. Section 4 provides an analysis of the impact of earthquakes on the

122 detector. Section 5 studies the impact of bad weather on data quality and duty cycle,  
123 disentangling contributions from sea activity and wind. Section 6 goes through other  
124 environment impacts: magnetic noise, lightning and a study of the cosmic muon rate on  
125 the Virgo central building. Then, Section 7 concludes this article by opening outlooks  
126 to the future O4 run. Finally, Appendix A provides a detailed and quite complete  
127 classification of the lock losses during the O3 run. Although that study has a scope  
128 broader than the present article, it is included here for reference and also because its  
129 results were used, in particular to find out which control losses were due to earthquakes.

## 130 2. The Virgo environmental monitoring during O3

131 The Virgo detector is equipped with a large set of probes used to monitor the conditions  
132 of the surrounding environment. Since these conditions can influence the detector  
133 response, or even mimic a GW event, it is very important to track their evolution,  
134 to assess the right working condition of the detector or to use them as veto against  
135 possible fake signals.

136 The set of probes and their conditioning electronics constitute the Environmental  
137 Monitoring System (EMS). The EMS was initially composed by a few tens of  
138 environmental probes (EPs) [19] and then improved during the detector upgrades that  
139 occurred in the past years. During O3, the total number of channels belonging to EMS  
140 was about 420.

141 The EMS is also helpful to understand the origin of some noise sources affecting the  
142 detector sensitivity. Indeed it was largely used during the commissioning phase following  
143 each detector upgrade, to recover and improve the Virgo performances in terms of  
144 sensitivity and duty cycle [11].

145 Data acquired for EMS can be grouped in two classes depending on the sample rate  
146 used for the different EPs. High-rate, or fast class includes those EPs acquired at  
147 rate up to 20 kHz like seismometers, piezoelectric (PZT) accelerometers, force balance  
148 (FB) accelerometer, magnetometers, microphones, voltage and current sensors, radio-  
149 frequency (RF) antennas, while low-rate or slow class includes temperature, pressure,  
150 humidity, weather and lightning probes, acquired at 1 Hz rate.

151 The main characteristics: type, model and frequency band of the EPs in use during O3  
152 are listed in Table 1. Figure 1 shows the arrangement of the EPs inside the main Virgo  
153 buildings. Most probes are located in the experimental halls of the relevant buildings  
154 of the detector: Central Building (CEB), North and West End Buildings (NEB and  
155 WEB) and Mode Cleaner Building (MCB). Usually, the probes are in contact with  
156 critical elements of the detector, like the walls of the vacuum chambers containing  
157 the test mass suspensions, or the optical benches hosting the laser injection and GW  
158 detection systems. Figure 2 shows a bird eye's view of the Virgo detector at EGO, with  
159 an emphasis on the location of the buildings that are identified in this article.

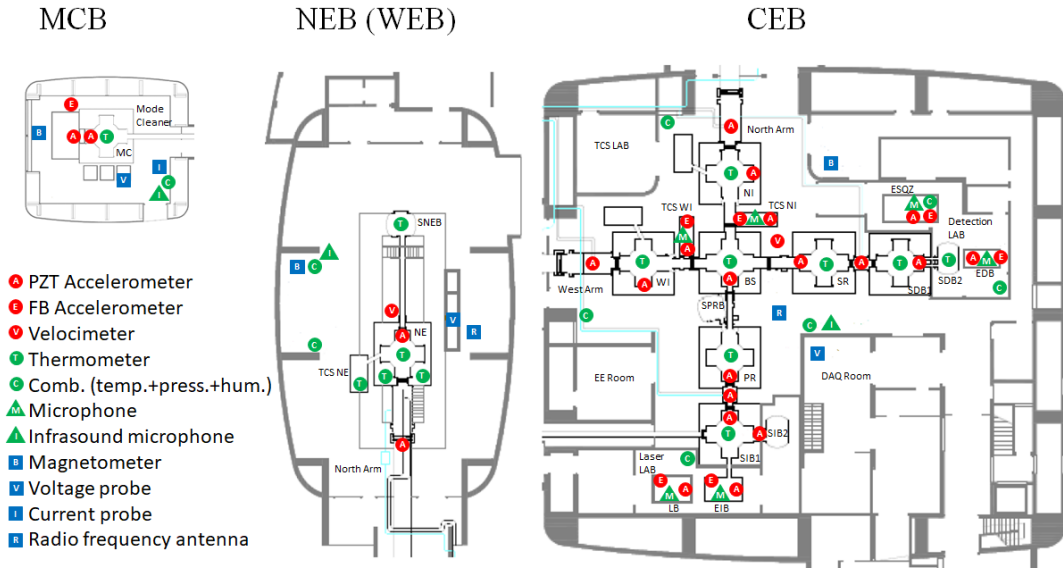


Figure 1: Location of the probes used for the Virgo environmental monitoring system. Maps of most relevant building are shown: left MCB, middle NEB, right CEB. The WEB is very similar to NEB and is not shown.

Type	Model	Frequency Band
Seismometer	Guralp CMG-40T	0.01 – 50 Hz
FB Accelerometer	Kinematics FBA ES-T	0.1 – 200 Hz
PZT Accelerometer	Wilcoxon 731-207 or PCB 393B12	1 – 1000 Hz
Magnetometer	Metronics MFS-06 or MFS-06e	0.1 mHz – 10 kHz
Microphone	Brüel & Kjær 4190 or 4193	0.1 – 10 kHz
RF antenna	AAS STA 5 A/D/0.01-100	10 kHz – 100 MHz
Voltage probe	Talema 0015P1-2-009	DC – 10 kHz
Current probe	IME 0015P1-2-009	DC – 10 kHz
Temperature probe	Analog Device AD590	DC – 0.5 Hz
Humidity probe	Honeywell HIH-5031-001	DC – 0.5 Hz
Pressure probe	NXP MPXA4115A6U	DC – 0.5 Hz
Weather station	Davis Advantage Pro 2	DC – 0.3 Hz
Lightning detector	Boltek LD 250	DC – 0.5 Hz

Table 1: Characteristics of the Virgo environmental probes during O3.

160 Few probes are placed outside the buildings and are not shown in the schematics,  
 161 namely the weather station, the lightning detector and two additional magnetometers.  
 162 These two low-noise induction coil magnetometers are deployed at 0.5 m depth in the  
 163 soil, at about 100 m from the CEB, oriented along the geographic North and West  
 164 directions. Their data are shared in real time with the <http://www.vlf.it> EM antenna  
 165 network [20].

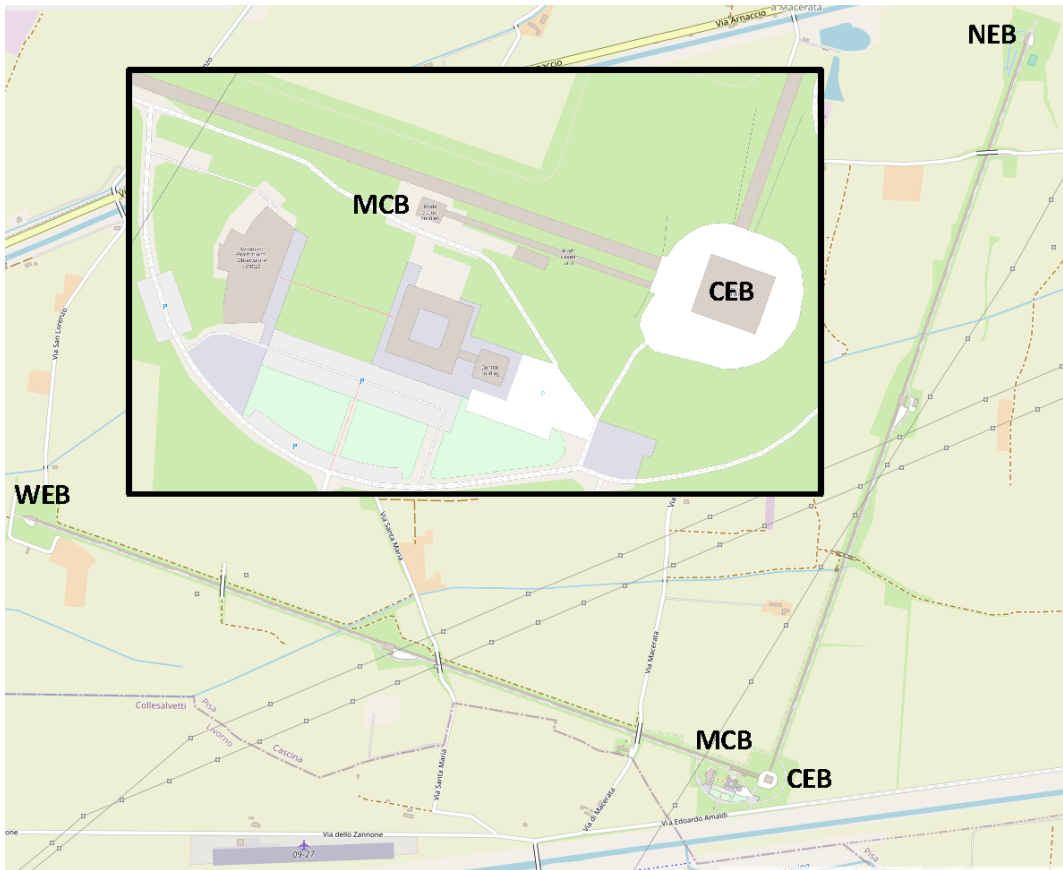


Figure 2: Map [21] of the EGO site showing the Virgo detector and in particular the location of the main buildings identified in the text. The central insert shows a zoom around the interferometer vertex, with the CEB and the MCB highlighted. The Mode-Cleaner cavity is 144 m-long while the Virgo arms are 3-km long.

### 166 3. Seismic noise

167 In this section we introduce the main sources of seismic noise at EGO. They are  
 168 disentangled and monitored by examining seismic probes in specific frequency bands.  
 169 We provide a statistical description of the noise and evidence its main recurring features.  
 170 Then, we describe how they impacted on the detector during the O3 run.

#### 171 3.1. The seismic frequency bands and their evolution during the O3 run

172 The seismic wavefield at EGO, the site of the Virgo detector, is the sum of several  
 173 sources [22]. Seismic spectrum variability during the O3 run is illustrated in Fig. 3. The  
 174 largest contribution to seismic ground motion in the frequency range between 0.1 Hz  
 175 and 1 Hz, referred to as *microseism*, is due to the interaction between shallow water sea  
 176 waves and the bottom of the sea [23, 24]. At EGO, the prevailing microseismic peak is  
 177 around 0.35 Hz.

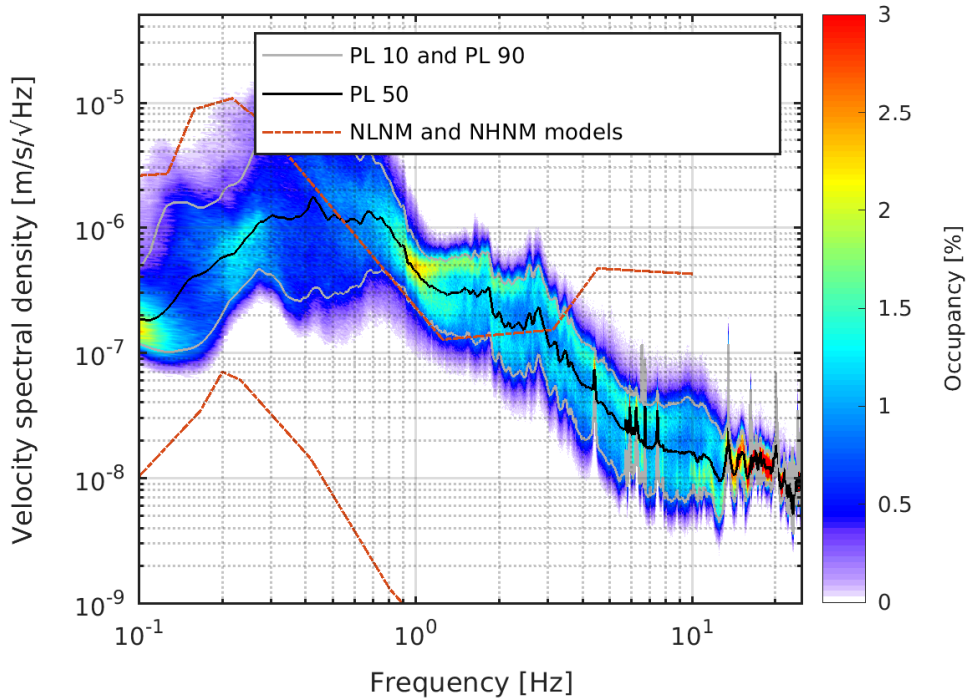


Figure 3: Variability of horizontal velocity of the Virgo NEB ground floor during O3. The quantity shown is the 2D histogram of the E-W velocity amplitude spectral density computed for the whole dataset recorded during O3 divided into 128 second long chunks. All interferometer maintenance periods are escluded from the computation. The color scale indicates the percent occupancy of histogram bins. The superposed continuous curves show different percentile levels (labelled *PL* on the plot): 10% (gray), 50% (black) and 90% (gray as well). The two red dashed curves correspond to the Peterson low-noise ('NLNM') and high-noise ('NHHM') models [25].

178 Figure 4 shows the time evolution of microseism during the O3 run, while Fig. 5 shows  
 179 the corresponding cumulative distribution, split by season. Microseism intensity follows  
 180 seasonal variations, being larger in fall and winter, due to the stronger wind and sea  
 181 activity.

182 Above 1 Hz, anthropogenic sources dominate the spectrum. Heavy vehicles (trucks and  
 183 alike) on  $\sim 1$  km distant elevated roads are the prevailing source of seismic noise in the  
 184 1-10 Hz band [22]. As illustrated in Fig. 6, the RMS of seismic noise in the 1-5 Hz band  
 185 follows a working day/night cycle with higher levels during working hours (from 8:00 to  
 186 17:00 local time – LT), with small reduction during lunch break (12:00-14:00 LT) and  
 187 minima during week-ends and holidays. The blue curve, used as reference, covers the  
 188 whole O3 run. The green curve is based on a 4-week period, from Monday 16 December,  
 189 2019 to Sunday 12 January, 2020: the noise reduction during the two consecutive  
 190 Wednesdays, Christmas 2019 and the New Year's Day 2020, is quite impressive. A



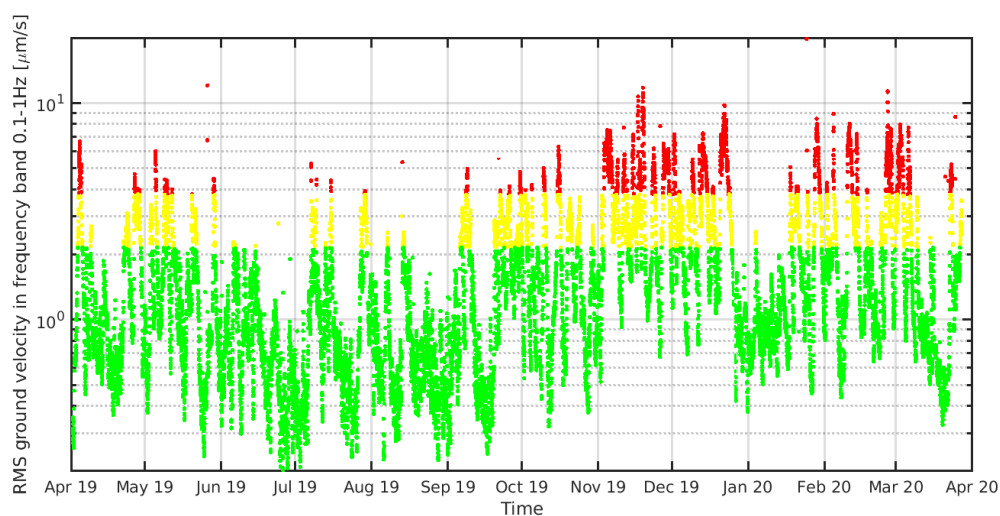


Figure 4: Evolution during O3 of seismic RMS in the 0.1 to 1 Hz frequency band. Data colored in yellow and red exceed the 75<sup>th</sup> and 90<sup>th</sup> percentile, respectively.

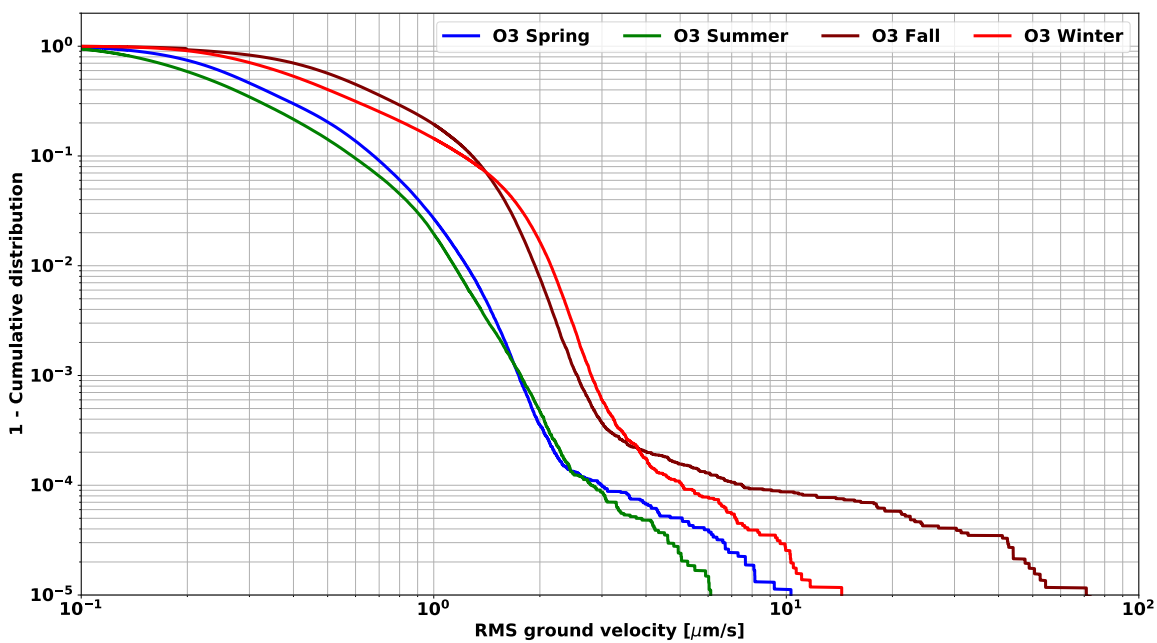


Figure 5: Cumulative distribution of microseism in the frequency band 0.1-1 Hz (dominated by sea activity), measured at EGO during each season in 2019-2020.

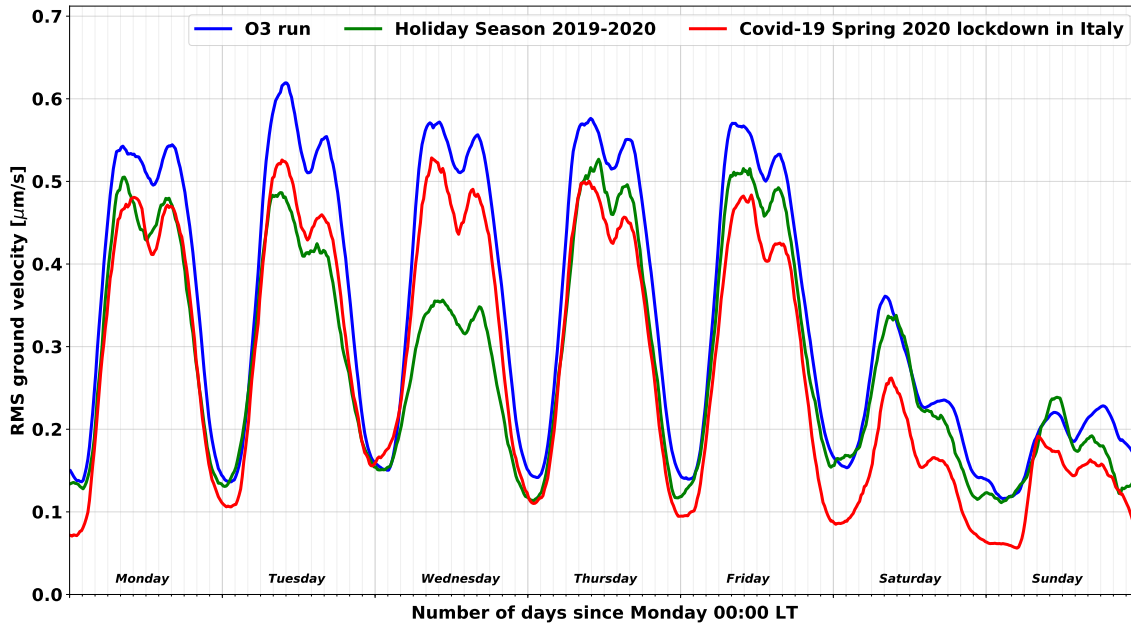


Figure 6: Average evolution on a weekly basis of the seismic anthropogenic noise (frequency band: 1-5 Hz) measured at EGO during different times in 2019-2020.

191 significant reduction of the anthropogenic noise is also visible during the Spring 2020  
 192 lockdown in Italy, due to the COVID-19 pandemic (red curve, covering a 8-week period  
 193 from 09 March to 03 May). That decrease is smaller than for the Christmas and New  
 194 Year holidays but it is more global as it is visible for all days of the week.

195 Finally, above 10 Hz, the dominant seismic contribution is generated locally: vehicles  
 196 in nearby and on-site roads, agricultural work on neighbouring land, etc. Figure 7  
 197 shows the average day-night variations, computed in the 10-40 Hz band on a weekly  
 198 basis: in blue during the O3 run; in magenta during the 1-month commissioning break  
 199 (October 2019) separating the two halves of O3; finally in orange for the second semester  
 200 of 2020, during which hardware upgrades and construction or infrastructure works for  
 201 the Advanced Virgo+ project [26] took place. The common feature between the three  
 202 curves is the dominant peak on Tuesday mornings, the usual slot used for the weekly  
 203 maintenance of the Virgo detector. This activity includes in particular the refilling of  
 204 Nitrogen ‡ tanks by heavy trucks coming on-site, and the possibility to have people  
 205 moving around and working inside experimental areas whose access is forbidden during  
 206 data taking periods. The on-site seismic noise level was slightly higher during the  
 207 commissioning break compared to the O3 run, but not by much: that shutdown was  
 208 not long enough to allow for invasive works that could have jeopardized the restart of  
 209 data taking on November 01, 2019, alongside the two LIGO detectors. On the other  
 210 hand, on-site activities are more evenly distributed over working days during the post-O3

‡ Liquid Nitrogen is used to cool down the Advanced Virgo cryotrap [2].

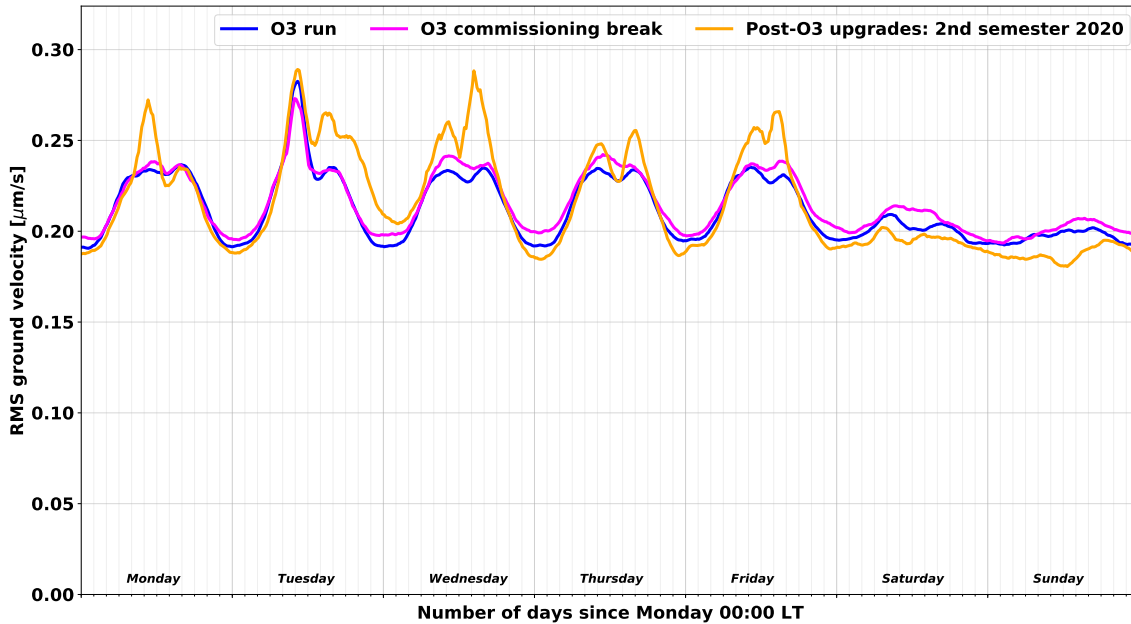


Figure 7: Average evolution on a weekly basis of the seismic on-site noise (frequency band: 10-40 Hz) measured at EGO during different times in 2019-2020.

211 upgrade. Though, activities were the lowest on weekends during that period because of  
 212 site access restrictions, enforced because of the pandemic.

### 213 3.2. Impact on the Virgo detector

214 The previous sections have demonstrated that the Virgo collaboration is accurately  
 215 monitoring the seismic environment at EGO and that the recorded data show significant  
 216 variations over time, in agreement with expectations from known noise sources. It is  
 217 then interesting to see how these noises impact the performance of the Virgo detector,  
 218 namely its sensitivity and duty cycle.

219 3.2.1. Sensitivity A convenient way to monitor the sensitivity of a gravitational-wave  
 220 detector like Virgo is to study the evolution of the *BNS range*, that is the average  
 221 distance up to which the merger of a standard binary neutron star system (BNS) can  
 222 be detected with a signal-to-noise ratio (SNR) set to 8, roughly corresponding to one  
 223 false alarm per year with purely Gaussian noise. The average is taken over the position  
 224 of the BNS in the sky and over the orientation of its orbital plane. Broadly speaking,  
 225 the lower (higher) the noise in the frequency band of interest –from a few tens of Hz to  
 226 a few hundreds of Hz depending on the actual sensitivity curve –, the larger (smaller)  
 227 the BNS range.

228 In addition to its potential dependence on the surrounding environment, the BNS range

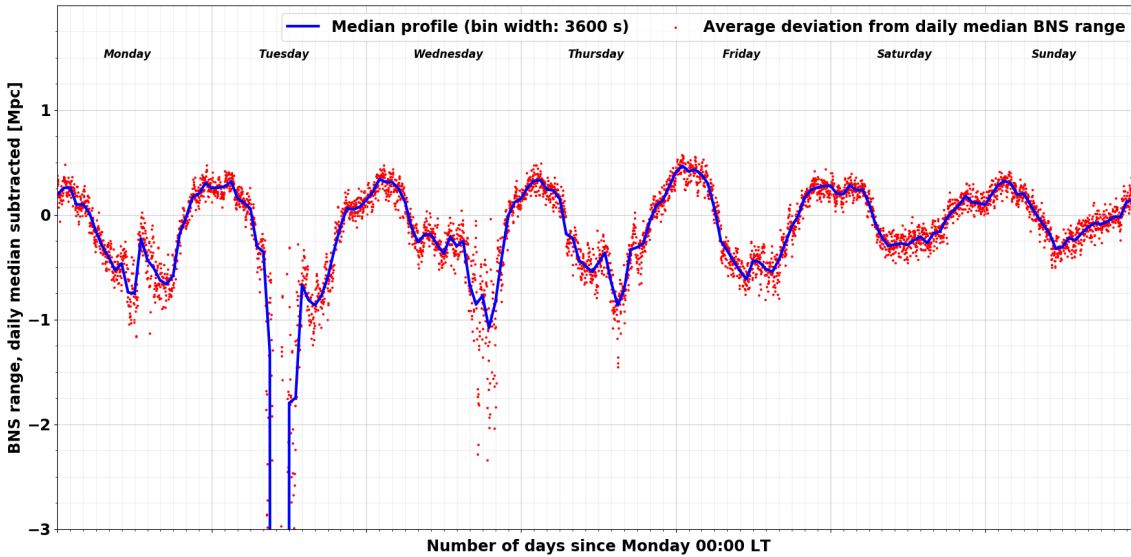


Figure 8: Average variation of the BNS range around its local average, computed on a weekly basis. The blue trace is a moving median profile of the red scatter plot, each dot showing the fluctuation at a particular weekday and time. The lack of available data on Tuesday morning corresponds to the weekly maintenance period of the Virgo detector, while the sharper variations on Wednesday and Thursday afternoons are due to the fact that these times have often been used for calibration or detector activities. Therefore, the BNS range is less stable than usually when nominal data taking gets restored.

229 can fluctuate significantly due to changes in the control accuracy of the detector.  
 230 Therefore, averaging raw BNS range values, especially over long timescales, is not  
 231 expected to provide meaningful information as one would mix together too many effects  
 232 that cause the BNS range to vary. Therefore, the method used in the following consists in  
 233 computing a moving daily average of the BNS range and to focus on the local fluctuations  
 234 around this level. Figures 8 and 9 show these variations, averaged over the whole O3  
 235 run, and projected over a weekly or daily time range, respectively. On both plots, the  
 236 red dots show daily variations while the blue curve is a moving median profile of the  
 237 scatter plot. The variations seen are clearly of anthropogenic origin, with a day-night  
 238 pattern and a reduced spread during the weekend. Although they are significant, they  
 239 are also limited in size:  $\sim 1$  Mpc compared to an average BNS range of about 50 Mpc  
 240 during the O3 run, hence a  $\sim 2\%$  fluctuation. This shows the robustness of the Virgo  
 241 detector.

242 *3.2.2. Duty cycle* Figure 10 shows the average duty cycle of the Virgo detector during  
 243 the O3 run. The top plot displays its average variation over a week, while the bottom one  
 244 focuses on a day. The red curve normalizes the Science mode data taking by the elapsed  
 245 real time, while the green one is computed by excluding the calibration, commissioning

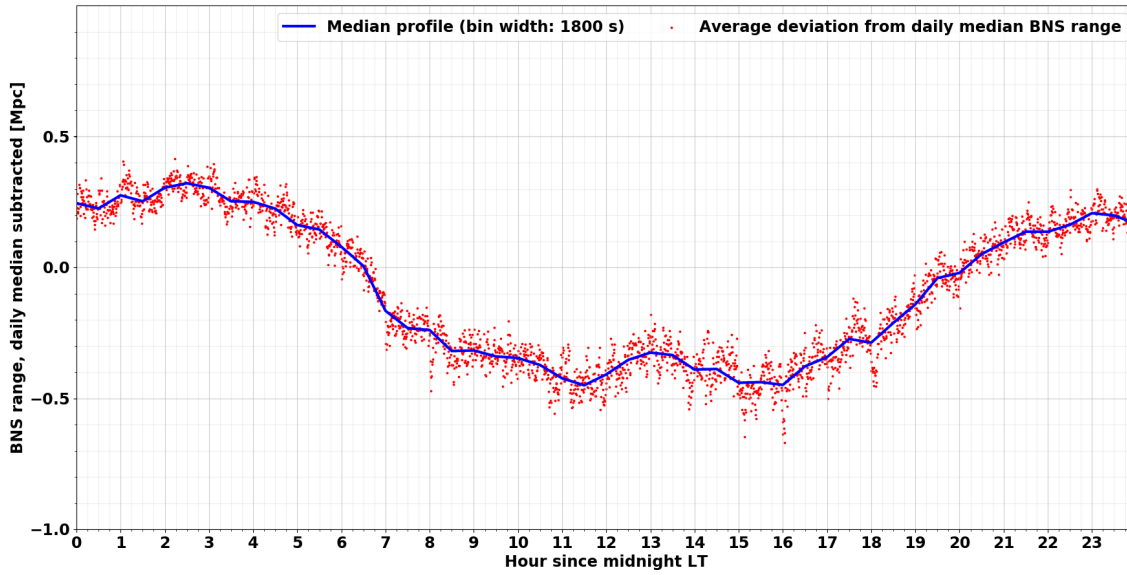


Figure 9: Average variation of the BNS range around its local average, computed on a daily basis. The blue trace is a moving median profile of the red scatter plot, each dot showing the fluctuation at a particular time of the day.

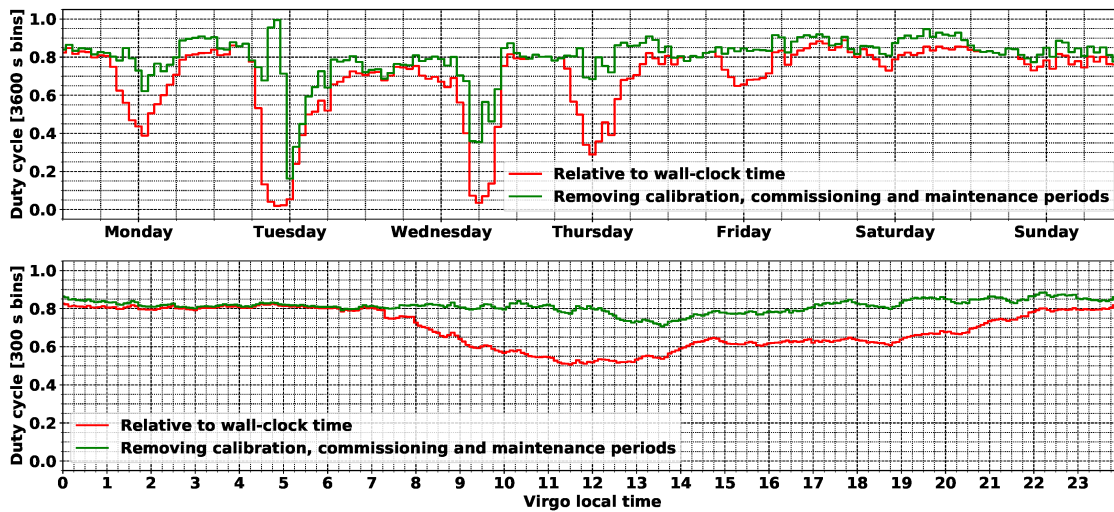


Figure 10: Average weekly (top) and daily (bottom) duty cycle of the Virgo detector during the O3 run. The red curve uses the elapsed real time as normalization, while the green one is produced excluding the times spent doing calibration, commissioning or maintenance, three activities that are incompatible with Science-mode data taking.

246 and maintenance periods. Thus, the latter curve shows the fraction of the time available  
247 for data taking that is actually used for that. Activities on the detector are concentrated  
248 during working hours as expected, with maintenance on Tuesday morning, calibrations  
249 on Wednesday evenings and commissioning slots from Monday to Friday depending on  
250 the needs. There is a non-negligible recovery time from maintenance, while the transition  
251 from calibration back to data taking is smoother and quicker on average. During the  
252 quietest hours of the night, when no work takes place on the interferometer except in  
253 case of an emergency, the average duty cycle reaches a plateau around 85%.

#### 254 4. Earthquakes

255 Earthquakes radiate energy through different types of seismic waves that are commonly  
256 divided in "body" and "surface" waves, depending on the path followed from the source  
257 to the receiver. Body waves that travel through the Earth are usually detected first.  
258 The fastest are named P-waves and are compressional longitudinal waves whose speed  
259 can reach 8 km/s. Then comes S-waves, transverse shear waves whose velocity scales  
260 by a factor of  $\sqrt{2}$  with respect to P-waves. Surface waves are slower and their size  
261 dominates at large epicentral distance since their amplitude scaling factor is 1/distance  
262 while body waves scale with  $1/\text{distance}^2$ . Most relevant surface waves are Rayleigh  
263 waves, that originate from P-wave and S-wave (with vertical polarization) coupling  
264 at the Earth surface. The result is a wave with both longitudinal and transversal  
265 components and a propagation speed up to a few km/s.

266 Since seismic waves excite buildings even at great distance, the Virgo monitoring set  
267 at EGO includes local, regional and teleseismic earthquakes since it was observed that  
268 all of them can induce large motion of the interferometer elements. This can saturate  
269 the control capability of the feedback systems that keep Virgo at its nominal working  
270 point, leading to a loss of control. Following each control loss (regardless of its origin:  
271 an earthquake or another cause), data taking stops immediately and can only restart  
272 after the completion of the semi-automated sequence that allows restoring the Virgo  
273 global working point – during the O3 run, that procedure took about 20 minutes on  
274 average [18]. But the time lost can be much longer in case of a control loss due to an  
275 earthquake, in case the suspension normal modes are excited by the seismic waves. In  
276 that case, one may have to wait up to one hour after the event that the high-quality  
277 factor modes of the suspensions are damped, before initiating the control acquisition  
278 procedure. Since each lock loss reduces the Virgo duty cycle, it is therefore important to  
279 understand which fraction of these are due to earthquakes, and what are the earthquakes  
280 that induce them.

281 Large earthquakes at local and regional scale do not happen very often, so the type  
282 of earthquakes on which this analysis is focused is large earthquakes that occur along  
283 the boundaries of the main tectonic plates. Most of them are quite distant from EGO,  
284 meaning that a low-latency framework relying on data from a variety of seismic stations

285 worldwide could produce early warning notices that would be received and processed  
 286 *ahead* of the seismic waves arrival. In that case, one could take preventive measures to  
 287 try to mitigate the effect of the ground shaking, with the goal of avoiding the lock loss.  
 288 In the following, we describe the strategy implemented at Virgo during the O3 run,  
 289 that relies on the Seismon framework developed at LIGO – an example of the existing  
 290 teamwork among members of the global GW detector network.

291 Furthermore, as explained below, the study has also highlighted another contribution  
 292 from much weaker earthquakes, quite close to EGO (the majority of which occur on the  
 293 Italian Apennines). Those have been more difficult to identify as they do not lead to  
 294 early warnings from Seismon and the frequency of their seismic waves is much higher  
 295 when they arrive at EGO: up to  $\sim 1$  Hz, whereas teleseism waves are in the frequency  
 296 band 10 – 100 mHz. In addition, the proximity of their epicenters makes useless the  
 297 use of warnings that would always come too late. Thus, the only way to mitigate these  
 298 earthquakes is to understand how they impact the Virgo control system and what could  
 299 be done to strengthen it.

#### 300 4.1. *Seismon and O3 setup at EGO*

301 In addition to making the whole detector as robust as possible against the passing of  
 302 strong seismic waves, the only other leverage one can use to mitigate the impact of  
 303 earthquakes is to rely on early warnings provided by worldwide arrays of seismometers.

304 Following initial tests done during the O2 run and the upgrade period that followed, we  
 305 ran at EGO during O3 an instance of the Seismon [27, 28, 29] framework, developed  
 306 by LIGO to process earthquake early warnings provided by the US Geological Survey  
 307 (USGS) [30] and to compute information relevant for each site of the LIGO-Virgo  
 308 network. Namely, for each earthquake, Seismon potentially predicts the arrival time  
 309 of the different seismic waves (P-, S- and surface), their amplitude at site and the  
 310 probability of losing the detector control in consequence of that earthquake. That  
 311 framework was split into four consecutive steps, each associated with a server integrated  
 312 within the EGO online data acquisition system (DAQ) used to steer and monitor the  
 313 Virgo detector.

- 314 • Reception of the USGS alerts.
- 315 • Processing of each alert by the Seismon framework.
- 316 • Extraction of the subset of Seismon data pertinent to the EGO site and provision  
 317 to the Virgo online framework.
- 318 • Local processing of these data.

319 In addition to producing a plot summarizing all information from the early warning,  
 320 a loose cut is applied on magnitude and distance to estimate whether the earthquake  
 321 could be relevant, meaning that it could impact the control of the Virgo detector. In

322 that case, and if the warning was quick enough to precede the arrival of the seismic  
323 wave on-site, an alarm would latch on the main panel of the Virgo Detector Monitoring  
324 System [31, 32], alerting the operator on duty in the control room.

325 In the nominal O3 control configuration, the two 3 km-long optical cavities are kept in  
326 resonance by acting on the end mirror suspensions: their actuators are the least noisy,  
327 at the price of a reduced correction range availability. Actuators located at the level  
328 of the input mirror suspensions have higher dynamics, while introducing slightly more  
329 noise. Thus, they can be used as earthquake control mode (in short *EQ mode*) to try  
330 to maintain the Virgo working point during periods of elevated seismic noise.

331 A smooth transition procedure, working both ways without losing the detector control,  
332 has been developed to allow switching back and forth between end-mirror and input-  
333 mirror actuations. During the O3 run, the procedure in use was the following: once  
334 alerted by Seismon, the operator on duty would monitor the optics suspension status  
335 and manually trigger the transition from nominal mode to EQ mode when the test mass  
336 suspensions would start shaking significantly. Once activated, that process would take  
337 a few tens of seconds to complete. Then, either the detector would nevertheless lose its  
338 working point (and the control acquisition procedure would have to be restarted from  
339 the beginning), or the EQ mode control would be kept until the whole seismic wave  
340 trains has passed by and the suspensions motion has been damped back to levels low  
341 enough to allow resuming the nominal control mode.

342 Unrelated to earthquakes, the EQ mode was also found useful during periods of high  
343 wind: gusts shake the building structures (walls and floors) and those vibrations can  
344 couple to the suspensions, potentially causing control corrections to saturate. However,  
345 since EQ mode was not validated for the production of good quality data for physics  
346 analysis, this was used parsimoniously during most of O3 because corresponding data  
347 would have to be discarded. A few weeks before the end of the run, the EQ mode got  
348 finally qualified for regular data taking and later studies [33] showed that there was no  
349 significant degradation of the Virgo sensitivity when switching to it. Therefore, it was  
350 used more regularly from that time; the possibility to have such a backup solution for  
351 O4 as well will be studied in the coming months.

#### 352 4.2. Earthquakes impact during O3

353 The stronger and/or the closer to EGO the earthquake, the more likely it is to impact  
354 the control of the Virgo detector. To study the impact of strong regional earthquakes  
355 or teleseisms, the USGS warnings processed by Seismon are sufficient (as they should  
356 include all such earthquakes). But it was soon realized that some moderate earthquakes  
357 occurring at local and regional distance (from few tens to few hundreds kilometers away  
358 from EGO), too weak to generate a USGS alert and then being processed by Seismon,  
359 could cause losses of control of Virgo. To check if any of these control losses was caused  
360 by this type of earthquakes, we queried [34] the INGV (Istituto Nazionale di Geofisica



361 e Vulcanologia) public earthquake catalogue [35] to download the list of events that  
 362 occurred during O3 in the Mediterranean region. This list partly overlaps with the  
 363 USGS one and duplicates were removed. All results presented in the following are based  
 364 on the whole set of earthquakes, assembled by merging the USGS and INGV event lists.

365 The control of the Virgo detector is extremely complex. Therefore, finding out how  
 366 many earthquakes induced control losses during the O3 run required a careful study  
 367 of all control losses, documented below in Appendix A. An earthquake from the list  
 368 of USGS warnings is associated to a recorded control loss if the loss occurs within the  
 369 time range during which seismic waves were predicted to arrive on-site according to  
 370 Seismon and if the seismic activity around the time of the control loss is significantly  
 371 larger than its typical range of variation. In case of concurring early warnings from  
 372 different earthquakes overlapping in time at EGO, the strongest is arbitrarily selected  
 373 as the reason for the control loss.

374 Estimating the strength of an earthquake when its seismic waves arrive at EGO is not  
 375 easy. Yet, this is a key point to address, first to reject quickly warnings from harmless  
 376 earthquakes and then to adjust the latency and level of response for the crew in charge  
 377 of steering the Virgo detector. During O3, basic rectangular cuts in the magnitude-  
 378 distance plane – e.g. *if magnitude > (...) or (distance < (...) km and magnitude >*  
 379 *(...)) or etc.* – were applied to the live earthquake warnings received from USGS and  
 380 processed by Seismon. During the post-run analysis, the ranking

$$\text{ranking} = \frac{10^{\text{magnitude}/2}}{\text{distance}[\text{km}]} \quad (1)$$

381 was introduced. While not complete – e.g. neither the hypocenter depth nor its azimuth  
 382 angle computed with respect to EGO are accounted for – this ranking appears sound:  
 383 the higher its value, the more likely the control loss. Applying a minimum cut at  
 384 ranking = 0.02 allows to safely remove more than half of the earthquakes to be analyzed.

385 Results shown below use the largest possible earthquake statistics, meaning that one  
 386 requires the Virgo detector to be fully controlled, but not necessarily in Science mode.  
 387 This looser requirement enlarges the dataset of interest and hence the number of  
 388 earthquake early warnings to be taken into account.

389 Figure 11 highlights the epicentral distance and magnitude of the earthquakes that led  
 390 to a Virgo control loss – called *delocks* in the captions. The top (bottom) row deals  
 391 with the earthquake magnitude (epicentral distance) while the right column displays  
 392 the ratio of the red and blue histograms shown on the left column. As expected, the  
 393 larger the earthquake magnitude, the more likely the control loss, with the fraction of  
 394 earthquakes leading to a control loss departing from 0 for magnitude 6 and above. That  
 395 fraction saturates to 1 (meaning that all events causes a control loss) when magnitude  
 396 exceeds 7.2. We also note that the fraction is not null around magnitude 3: this reflects  
 397 the control loss consequence of some small local earthquakes recognizable also in the left

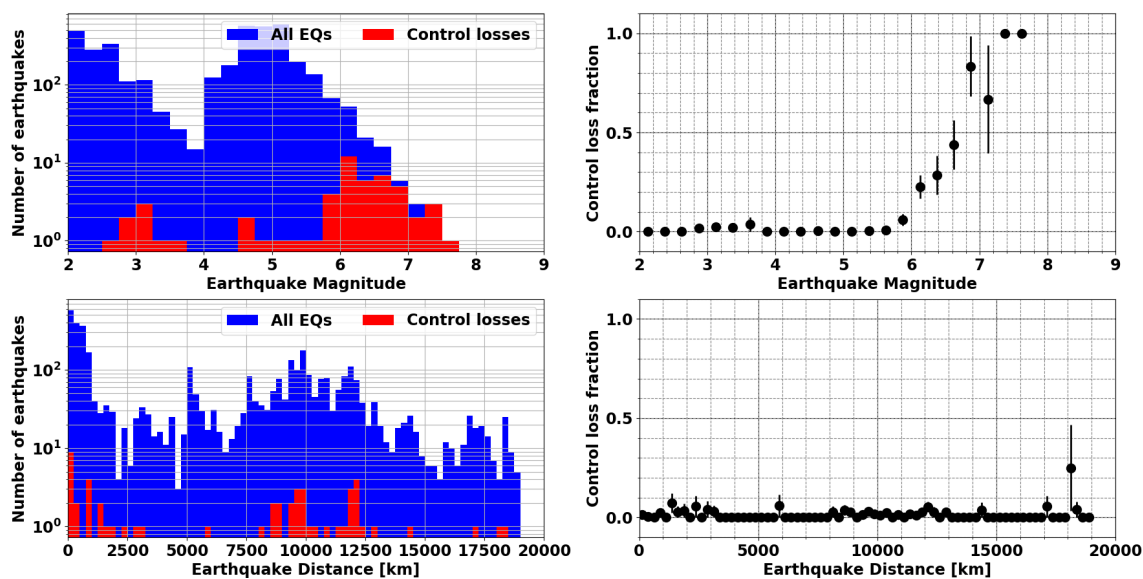


Figure 11: Summary of the impact of earthquakes on the Virgo detector during the O3 run. Left column: the blue (red) histogram shows all earthquakes (the earthquakes that have induced a control loss); top: magnitude distribution; bottom: distribution of the distance between EGO and the epicenter. Right column: corresponding fraction as a function of the earthquake magnitude (top) and distance (bottom). In all cases, the earthquakes that certainly could not impact Virgo (ranking below 0.02) were excluded.

398 side histogram of Figure 11. The histogram ratio is much flatter for that other variable,  
 399 with the most significant bins reflecting the location of seismic regions on the globe with  
 400 respect to EGO, mainly the broad Mediterranean area and the Ring of Fire (a region  
 401 covering much of the rim of the Pacific Ocean that is seismically very active).

402 Figure 12 shows the population of earthquakes that caused a control loss (red dots) in the  
 403 two-dimensional plane epicentral distance vs. magnitude. These earthquakes form the  
 404 upper envelope of the scatter plot drawn, meaning they are usually the earthquakes with  
 405 largest magnitude for any distance. The separation between red and green (earthquakes  
 406 that did not cause a control loss) dots is not perfect for at least two reasons. The first  
 407 one is that the control of the Virgo detector is complex enough that the actual level  
 408 of control (accuracy and stability) plays a role in whether or not the control is lost  
 409 for earthquakes at the limits of inducing a control loss. The second reason is that our  
 410 model could probably be improved by including other earthquake warning parameters:  
 411 two candidates would be the hypocenter depth (the deeper the hypocenter, the lower  
 412 the earthquake impact on the ground at equivalent magnitude) and the azimuthal  
 413 orientation of the epicenter with respect to EGO.

414 L405 and following, I would write ?...show the location of the significant earthquakes that  
 415 occurred during O3 with the same color coding used in Figure 11. Their distribution  
 416 depicts the boundaries of the main tectonic plates and, as discussed above, we can

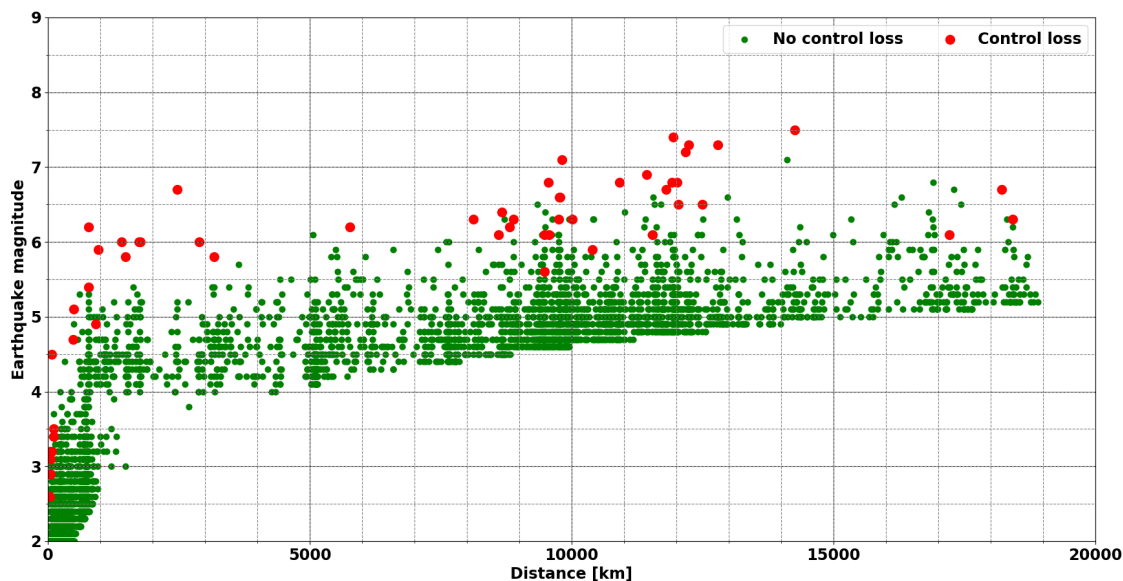


Figure 12: Distribution of earthquakes in the plane distance-magnitude during the O3 run. The earthquakes that caused a control loss (did not cause a control loss) are represented with red (green) dots. The lack of points below the main bulk of earthquakes is due to the ranking cut, set at 0.02.

417 observe that the most harmful??

418 Figures 13 and 14 show the location of the significant earthquakes that occurred during  
 419 O3 with the same color coding used in Figure 12. Their distribution depicts the  
 420 boundaries of the main tectonic plates and, as discussed above, we can observe that the  
 421 most harmful earthquakes for Virgo are coming from the Mediterranean area (medium  
 422 to large magnitudes but smaller distances) and part of the Pacific Ring of Fire. The mid-  
 423 Atlantic ridge and the Asian portion of the Alpidic earthquake belt did not produce many  
 424 earthquakes that impacted Virgo, possibly because of the limited statistics. During the  
 425 O3 run, the distribution of the earthquakes leading to control losses was the following:  
 426  $\sim 15\%$  of close earthquakes;  $\sim 20\%$  from other earthquakes in the Mediterranean area;  
 427 and  $\sim 65\%$  from distant earthquakes. We remark that this statistics has not an absolute  
 428 meaning: the O3 run took place during a quiet seismic period for Italy, compared to  
 429 e.g. 2009 or 2016. This analysis will be updated in the future with data from the O4  
 430 run.

431 Finally, Fig. 15 shows an example of the impact of a strong and distant earthquake  
 432 on the Virgo detector and how the early warning information was used to change the  
 433 control mode prior to the arrival of the strongest seismic waves allowed to keep the  
 434 working point of the instrument by preventing the correction force (applied on mirror  
 435 suspensions to maintain resonance in the arm cavities) from saturating. Should that  
 436 action not have been performed, the control loss would have been unavoidable – as the  
 437 correction would have saturated around 22:27 UTC. The description of the different

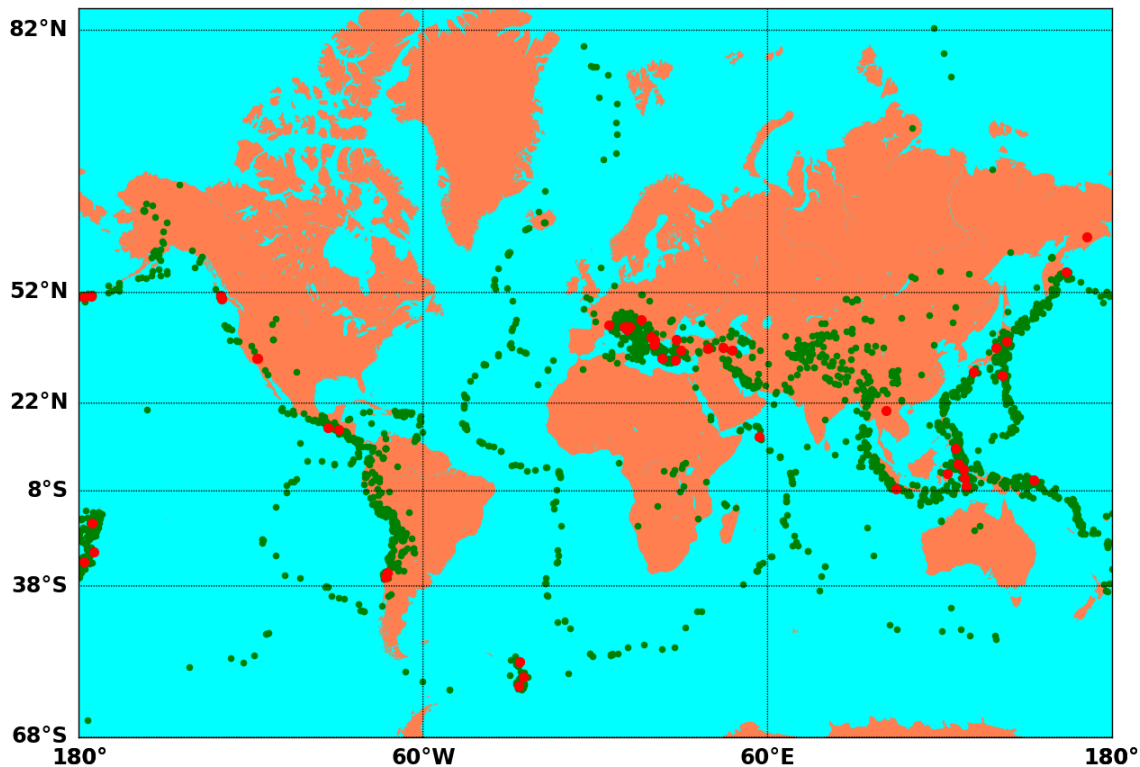


Figure 13: Location of the O3 earthquakes used in this study (ranking greater than 0.02) The earthquakes that caused a control loss (did not cause a control loss) are represented with red (green) dots.

438 stripcharts displayed is given below.

- 439
- 440 • Top plot: variation of the index labelling the Virgo data taking configuration – the  
441 Science mode – corresponds to the value 1; other indices shown here (-1, -7, -9)  
442 indicate other control configurations that are not nominal and that were used to  
443 wait for the right moment to switch back to Science data taking mode.
  - 444 • Second plot: stripchart of the BNS range versus time; the seismic waves clearly  
445 make the BNS range go down and fluctuate more while they are passing (see seismic  
446 activity variations recorded in the bottom plot, described below); the BNS range  
447 recovers its steady value at the end of the plotted time when the earthquake effect  
448 fades away.
  - 449 • Third plot: switch showing the times when the earthquake-resilient control mode  
450 ('EQ-mode') is turned on (0 → 1 transition) and later on off (1 → 0 transition)  
451 manually.
  - 452 • Fourth plot: For each second, maximum value of the correction applied on the test  
453 masses to keep the Virgo arms in resonance. When the nominal control mode is  
454 used, a control loss happens within two seconds at most after the time for which

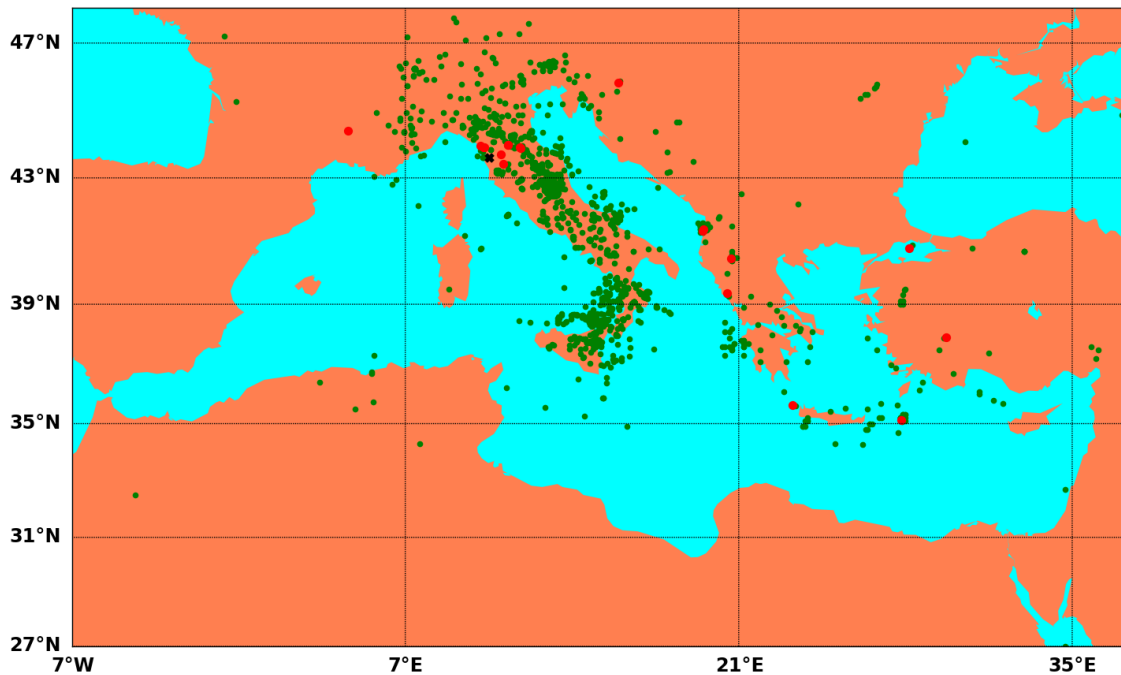


Figure 14: Zoom on the Mediterranean area of the map shown in Fig. 13 above. It shows the earthquakes nearby Virgo (whose site, EGO, is marked by a black cross) recorded during the O3 run. The earthquakes that caused a control loss (did not cause a control loss) are represented with red (green) dots.

454 the correction voltage§ exceeds a 9.5 V threshold. This occurs a few times close to  
 455 the middle of the time range represented here but no control loss follows, as the  
 456 EQ-mode allows for larger corrections.

- 457 ● Bottom plot: seismic noise measured in three orthogonal directions (vertical and  
 458 along the two Virgo arms) using the dominant frequency range for earthquakes  
 459 recorded at teleseismic distance: 10 mHz  $\rightarrow$  100 mHz.
- 460 ● Finally, the vertical dashed lines common to all plots show the time of important  
 461 events. From left to right: the time at which the earthquake occurred; the time  
 462 at which the corresponding USGS warning had been received and processed by  
 463 the Seismon framework; the expected arrival time of the seismic P-waves, S-waves  
 464 and Rayleigh waves. For the latter, we three different arrival times that stem from  
 465 different used velocities (5, 3.5 and 2 km/s respectively).

466 dominant frequency range for earthquake recorded at teleseismic distance?

§ The mirror control is done by varying the amount of current applied to actuators (pairs of coil-magnet): see Ref. [16] for details.

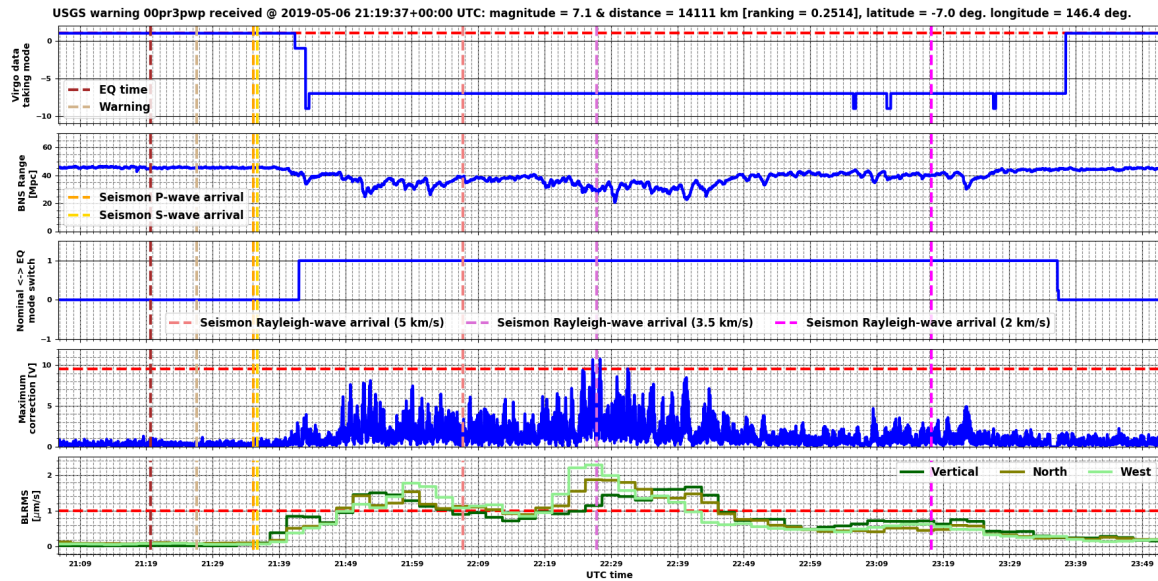


Figure 15: Example impact on the Virgo detector of a strong (magnitude greater than 7) and distant (14,000 km away from EGO) earthquake, that occurred on May 06, 2019 at 21:19:37 UTC in Eastern Papua New Guinea. The description of the different stripcharts is provided in the text.

#### 467 4.3. Plans for O4

468 Work is in progress to build on the O3 experience and have a more performing, better  
 469 integrated, earthquake early warning framework for O4 (and beyond). The plan is  
 470 to run the latest version of Seismon with an improved prediction capability for EGO,  
 471 achieved by means of all the data collected during the O3 run. We are also exploring  
 472 the possibility to use the INGV Early-Est system (a framework for rapid location and  
 473 seismic/tsunamigenic characterization of earthquakes) [36, 37] as an additional source  
 474 of warnings, complementary to USGS. Tests are in progress to have this new live stream  
 475 received at EGO and integrated into the existing framework. The two sets of early  
 476 warnings will then be compared, in terms of latency and accuracy.

#### 477 5. Bad weather

478 Through O3, the Virgo interferometer performed worst during days with adverse  
 479 meteorological conditions, namely high winds and intense sea activity. These periods  
 480 were generally associated with increased non-stationary noise in the GW signal below  
 481 about 100 Hz and with some difficulties in maintaining the interferometer in the  
 482 controlled state, resulting in reduced duty cycle. In the following, we study the impact  
 483 of the increased microseismic noise associated to sea waves, then the influences of wind  
 484 on BNS range, as well as the effect of wind gusts on the global interferometer controls.

485 Because of the wind action on the sea surface, high winds and rough sea often occur  
 486 together. We use a statistical approach to disentangle their effects on the detector.

### 487 5.1. Impact of sea activity

488 Microseism amplitude at EGO increases by more than one order of magnitude between  
 489 calm and rough sea periods. For 10% of the time during O3, ground RMS velocity  
 490 between 0.1 Hz and 1 Hz was above 4  $\mu\text{m/s}$ , as shown in Fig. 5. This happened in  
 491 particular in correspondence of the seasonal change in the first part of O3b and for some  
 492 periods of adverse weather condition in the first months of 2020. Periods of intense sea  
 493 activity were associated to larger than usual strain residual noise whose characteristics  
 494 and origin require further analysis.

5.1.1. *Microseism impact on strain noise* Periods of high sea activity were associated with larger strain residual noise up to about 100 Hz. To characterize this effect, we made use of the *band-limited* RMS (BLRMS), defined for a generic signal, in a certain frequency band  $[f_{\min}, f_{\max}]$ , as:

$$\text{BLRMS}(t; [f_{\min}, f_{\max}]) := \sqrt{\int_{f_{\min}}^{f_{\max}} S(f; t) df} \quad (2)$$

495 where  $S(f; t)$  is an estimate of the signal *power spectral density* (PSD) referred to a time  
 496  $t$ .

497 In Fig. 16, we report, for the entire O3 run, in blue the BLRMS of the strain in the band  
 498  $[10, 20]$  Hz and, in red, the CEB seismometer BLRMS in the band  $[0.1, 1]$  Hz. These have  
 499 been estimated from (2), where  $S(f; t)$  is computed with the Welch’s method making  
 500 use of strides of 2048 seconds and FFT length of 128 seconds, overlapping by 50% [38].  
 501 The correlation between the two curves is apparent. In particular, when the microseism  
 502 is intense, the peaks in the strain BLRMS are almost everywhere coincident with those  
 503 in the seismometer BLRMS. This fact is also highlighted in the 2D-histograms on the  
 504 right-hand side of the same figure, where the Pearson correlation coefficient has been  
 505 computed for the two data taking periods, O3a (top) and O3b (bottom). In general,  
 506 we observe that, despite the “spikes” in correspondence of bad weather conditions (in  
 507 particular at the beginning of O3b and then during most of Winter||), the induced strain  
 508 noise at low frequency has improved during O3 and can now be mostly attributed to  
 509 microseism.

510 5.1.2. *Microseism impact on glitch rates* Besides an increase in the RMS value of the  
 511 strain noise at low frequency, microseisms induce short transients of power excess in  
 512 this signal, colloquially referred to as *glitches*. In Fig. 17 we report the minute rate of

|| That calendar season starts around day 50 of O3b and lasts almost until the end of the data taking.

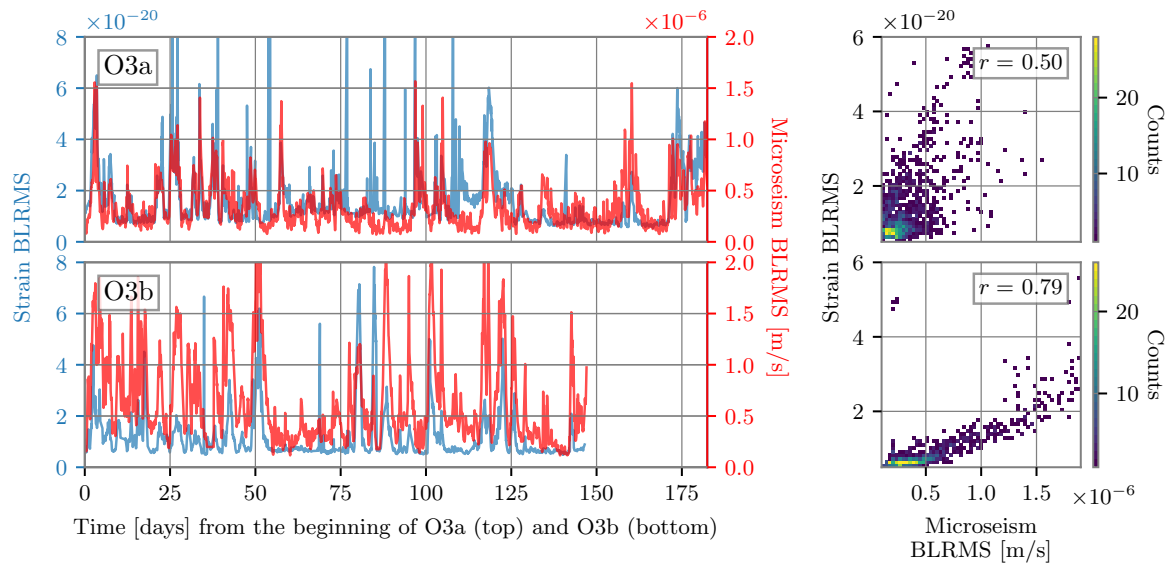


Figure 16: Correlation between the low frequency noise in Virgo GW strain and the microseism induced by the sea activity; top row for for O3a and bottom for O3b. Left: in blue the time series of the strain BLRMS in band  $[10, 20]$  Hz and in red that of the BLRMS in band  $[0.1, 1]$  Hz of a CEB seismometer, mostly influenced by the sea activity. Right: 2D-histograms of the correlation between the two BLRMS, where the colorscale counts, for every pixel in this map, how many data points have the corresponding values of strain and microseism BLRMS. The annotations in the top-right corners report the values of their Pearson correlation coefficient  $r$ .

513 these glitches during the entire O3 run. To reduce the – usually very large – variability  
 514 in their rate, we computed running daily medians. The gray dashed line represents the  
 515 time evolution of daily medians for glitches with  $\text{SNR} > 6.5$  and frequency at peak  
 516 in the band  $[10, 2048]$  Hz, as measured by the Omicron pipeline [39]. The blue solid  
 517 line is the median minute rate of glitches with peak frequency in the  $[10, 40]$  Hz band.  
 518 These glitches accounted for about 30% of the total during O3a, and for almost 40% in  
 519 O3b, with peaks larger than 80% in correspondence of periods of intense sea activity.  
 520 This glitch rate is highly correlated with microseism, represented in the left-hand side  
 521 plot of Fig. 17 by the solid red line of the running weekly median of the BLRMS in  
 522 band  $[0.1, 1]$  Hz of the CEB seismometer. On the right-hand side of the same figure, we  
 523 report the 2D-histogram of these two quantities and the value of their Pearson coefficient  
 524 ( $r = 0.91$ ).

525 *5.1.3. Microseism and scattered light* Glitches due to microseism often resemble arches  
 526 in a time-frequency map, as illustrated for example in Fig. 18. Arches are the typical  
 527 signature of scattered light (SL) noise processes, which is a major issue and topic of  
 528 investigation in the second generation GW detectors [11, 12, 13, 40, 41, 42].



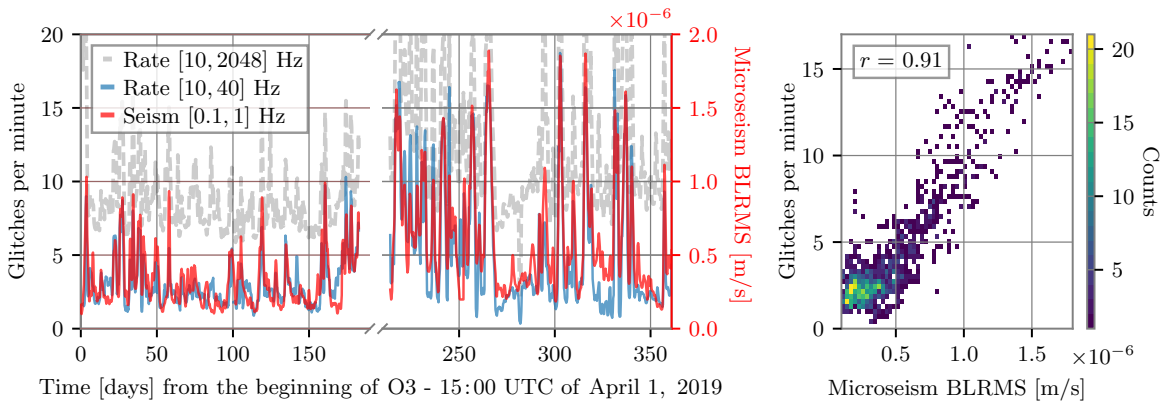


Figure 17: Correlation between Virgo glitch rate and the sea induced microseism during the O3 run. Left: the dashed gray line represents the daily moving median of the glitch rate per minute recorded by Omicron [39] for glitches with SNR > 6.5 and frequency at peak in band [10, 2048] Hz, estimated over strides of 2048 seconds. The blue continuous line is the median rate referred to glitches with frequency at peak in [10, 40] Hz band. The continuous red line is the BLRMS in band [0.1, 1] Hz of a seismometer in the Virgo CEB. Right: 2D-histogram of the glitch rate in band [10, 40] Hz and the microseism BLRMS, where the colorscale counts, for every pixel in this map, how many data points have the corresponding values of the rate and the microseism BLRMS. The annotations in the top-right corners report the values of their Pearson correlation coefficient  $r$ .

529 A stray light beam bouncing off a moving surface adds constructively to the beam main  
 530 mode every time its optical path,  $x(t)$ , changes (increases or decreases) by an integer  
 531 wavelength. It follows that the frequency of the strain noise is:

$$f_{sc}(t) = \frac{2n|\dot{x}(t)|}{\lambda} \quad (3)$$

532 where  $\dot{x}(t)$  is the instantaneous relative velocity between the interferometer beam and  
 533 the scatterer, and  $\lambda = 1.064 \mu\text{m}$  is the Virgo laser wavelength. Equation 3 is referred  
 534 to as predictor. In case the scattered beam encounters a second reflective surface it can  
 535 bounce back and forth  $n$  times along the same path before recombining, giving rise to  
 536 higher order noise arches, reaching out  $n$ -times larger frequencies.

537 In O3 the main sources of scattered light affecting the sensitivity were the suspended  
 538 optical benches placed beyond the end test masses in the terminal buildings (SNEB,  
 539 SWEB). In this case, the noise observed in the time-frequency domain is well visible as  
 540 power fluctuations in the cavity. The noise appears as a series of arches, where the typical  
 541 non-stationarity and non-linearity of the noise is evident. Arch time spacing is the half-  
 542 period of the oscillation of the mirror-bench relative motion, and arch amplitude (i.e.  
 543 the maximum frequency extension of the induced strain noise) is  $f_{max} = (4\pi/\lambda)AFn$   
 544 where  $A$  and  $F$  are the amplitude and frequency of the oscillation. If the frequency

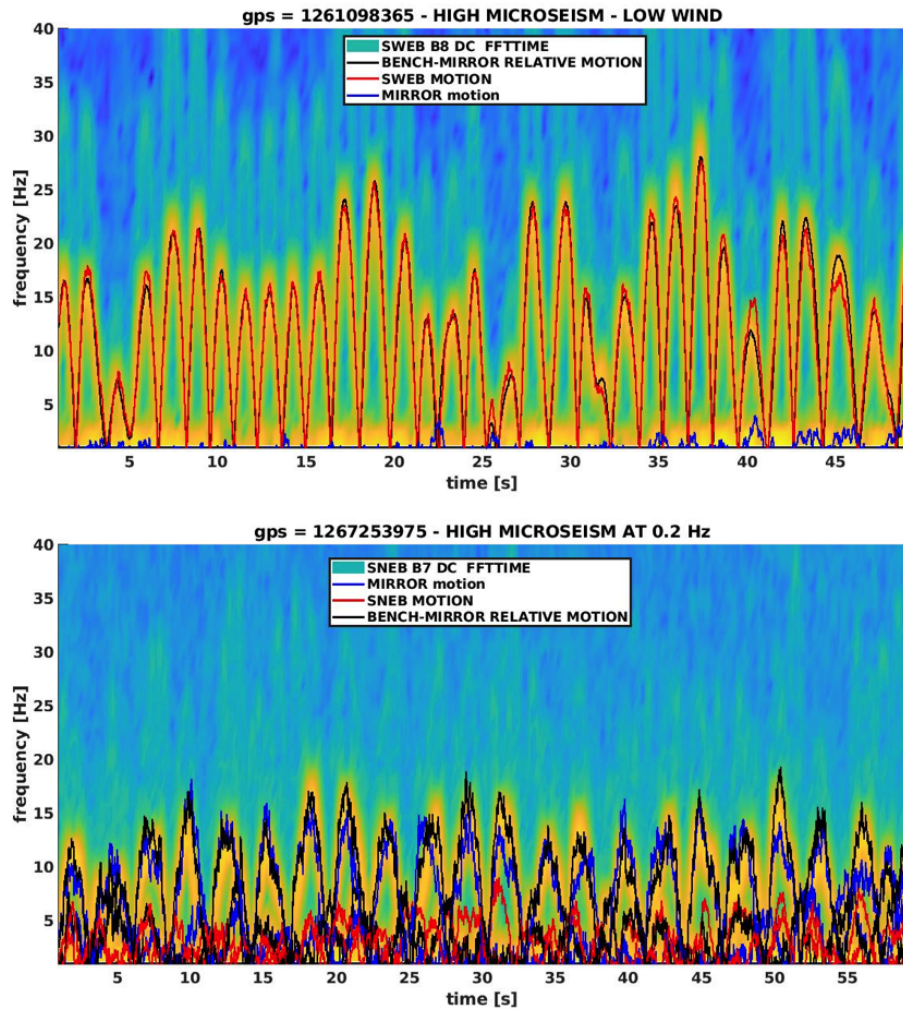


Figure 18: Spectrograms of the light transmitted at the end of the arm cavities and detected by photodiodes located behind, on suspended benches – top plot: west arm, B8 photodiode, SWEB bench; bottom plot: north arm, B7 photodiode, SNEB bench. The typical pattern of scattered light noise (arches) – both first order and second order (higher frequencies) – is visible. On the SWEB plot, arch spacing and amplitude correspond to half the period of marine microseism at Virgo ( $\sim 3$  s) and a ground velocity of about  $8 \mu\text{m/s}$ . The predictor for BENCH-MIRROR is shown in black, while the predictors computed from mirror and bench motions are shown in blue and red, respectively. The overlap shows that BENCH-MIRROR is the best predictor of scattered light, closely matching the observed arches.

545 and amplitude of the oscillation are such that  $f_{max} > 10$  Hz, the noise affects the GW  
 546 detection frequency band.

547 Being those benches suspended and controlled [43], their motion induced by the  
 548 microseism was supposed to be attenuated enough to push the maximum frequency of  
 549 the arches below 10 Hz. Moreover, a control technique taking into account the mirror-

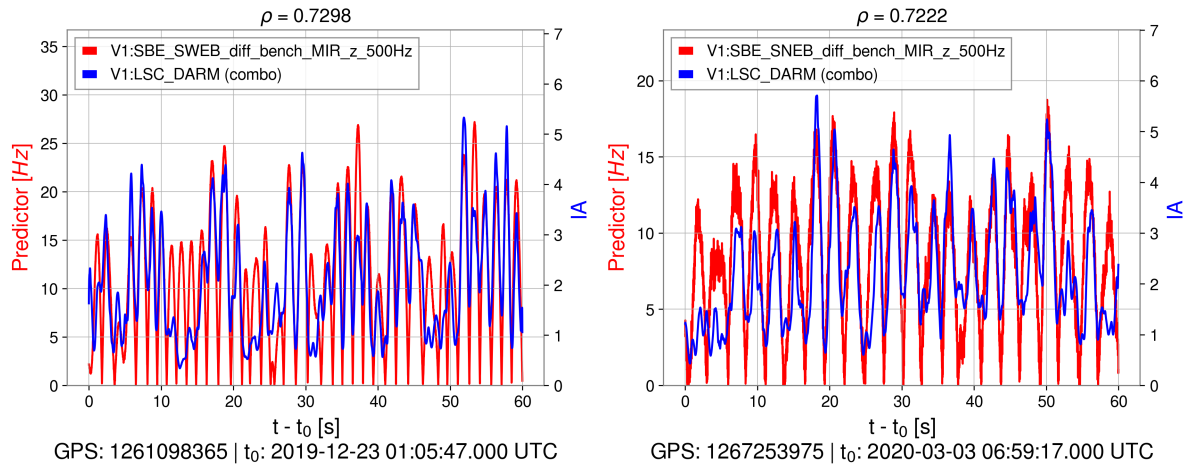


Figure 19: In red is the culprit’s predictor, i.e. Equation 3 for the relative motion (diff) between the suspended end bench and the end mirror (BENCH-MIRROR) of the West end (left) and North end (right). The sum of the IA of the first two modes of DARM, extracted by tvf-EMD is shown in blue.

550 bench differential signals was implemented in order to reduce their relative motion  
 551 (BENCH-MIRROR), which is the quantity effectively responsible of the noise coupling.

552 During O3, a malfunctioning was identified in the mechanical setting of the West  
 553 Bench suspension (SWEB) which caused its actual motion to be comparable to the  
 554 ground motion at the frequency of the main microseismic peak. Figure 18 shows the  
 555 mirror contribution and the bench contribution to the arches separately, for both North  
 556 and West cavity, in two selected bad-weather conditions. In the West arm power  
 557 spectrogram, the typical pattern is visible: the arches were entirely due to SWEB  
 558 motion, and all the times the ground motion exceeded a certain threshold during the  
 559 run, these arches entered the detector band. In the North arm power spectrogram, the  
 560 arches were normally much lower, and the contribution from the bench motion was of  
 561 the same magnitude as the mirror motion. It was even possible to find some special  
 562 conditions (the largest component of the ground motion centered at 0.2 Hz), in which  
 563 the mirror motion was prevalent (see Figure 18, bottom panel).

564 The issue concerning SWEB mechanics and control has been understood and cured after  
 565 O3. In O4, its residual motion is expected to be at least similar to the one observed in  
 566 O3 for SNEB. Further improvements in the control strategy will be tested for both the  
 567 mirror and the bench suspension.

568 *5.1.4. Identification of scattered light culprits* Part of the effort regarding scattered  
 569 light noise mitigation consists in the localisation of scattered light sources, referred  
 570 to as culprit, through data analysis. This can be a difficult and time consuming  
 571 operation in a km-long detector with many possible sources of SL. Adaptive algorithms

572 for time series analysis can be used to this end, due to their ability to decompose  
 573 nonlinear non-stationary data into a set of oscillatory modes [44, 45]. The methodology  
 574 described in [45] and based on the time varying filter empirical mode decomposition (tvf-  
 575 EMD) [46] adaptive algorithm is applied to the two data segments shown in Fig. 18.  
 576 SL noise couples with the differential motion of the arm cavities (*DARM*, the Virgo  
 577 longitudinal degree of freedom sensitive to GW) time series, which is first low-passed  
 578 and then decomposed using tvf-EMD to extract its oscillatory modes, from which the  
 579 instantaneous amplitude (IA) is obtained using the Hilbert transform. Computing  
 580 Equation 3 for a broad list of position sensors and correlating with the IA of *DARM*'s  
 581 oscillatory modes allows to quickly identify the most correlated channel, i.e. the culprit.  
 582 The two data segment considered are

- 583 • GPS: 1261098365 UTC - 2019/12/23 01:05:47 + 60s,
- 584 • GPS: 1267253975 UTC - 2020/03/03 06:59:17 + 60s.

585 Obtained results are reported in Fig. 19, showing the predictors of the culprit for the end  
 586 benches, based on Equation 3, correlated with the IA of *DARM*. The culprits are related  
 587 to the *BENCH-MIRROR* channel in both cases. The resulting values of correlation are  
 588  $\rho = 0.73$  for *SWEB* and  $\rho = 0.72$  for *SNEB*. Since after low-passing the data the first  
 589 two oscillatory modes of *DARM* were found to be the most correlated with the same  
 590 predictor, the sum of their IA is considered and is shown in Fig. 19 for both cases,  
 591 referred to as *combo*. As a counter proof, in Fig. 18 the predictors of the culprits are  
 592 overlapped on the spectrograms of the *WEB* and *NEB* photodiodes. It can be seen  
 593 that they closely match the scattered light arches. In particular, for the *SWEB* case,  
 594 the mirror motion is small and the bench motion is mainly responsible for the observed  
 595 scattered light. For *SNEB* case, while the mirror motion is significant the *BENCH-*  
 596 *MIRROR* predictor, identified with adaptive analysis, better matches the arches also in  
 597 this case.

## 598 5.2. Impact of wind

599 Figure 20 summarizes the wind statistics recorded at *EGO* during the *O3* run. Wind is  
 600 blowing more often from the East while the stronger winds are predominantly coming  
 601 from the West – the sea shore.

602 The method described in Sec. 3.2.1 can be applied to quantify the impact of the  
 603 instantaneous wind speed on the sensitivity. Figure 21 shows that the sensitivity is  
 604 pretty much unaffected until a wind speed of  $\sim 20 - 25$  km/h, while the detector gets  
 605 sensitive to larger speeds: the *BNS* range decrease exceeds  $\sim 4$  Mpc for a wind speed  
 606 of 50 km/h or above. Yet this variation is limited (about 10% of nominal *BNS* range  
 607 values during *O3*), meaning that the detector is quite robust against wind. Another  
 608 consequence of high-wind conditions is the need for the *Virgo* global control system to  
 609 use larger corrections to keep the instrument at its nominal working point. And the

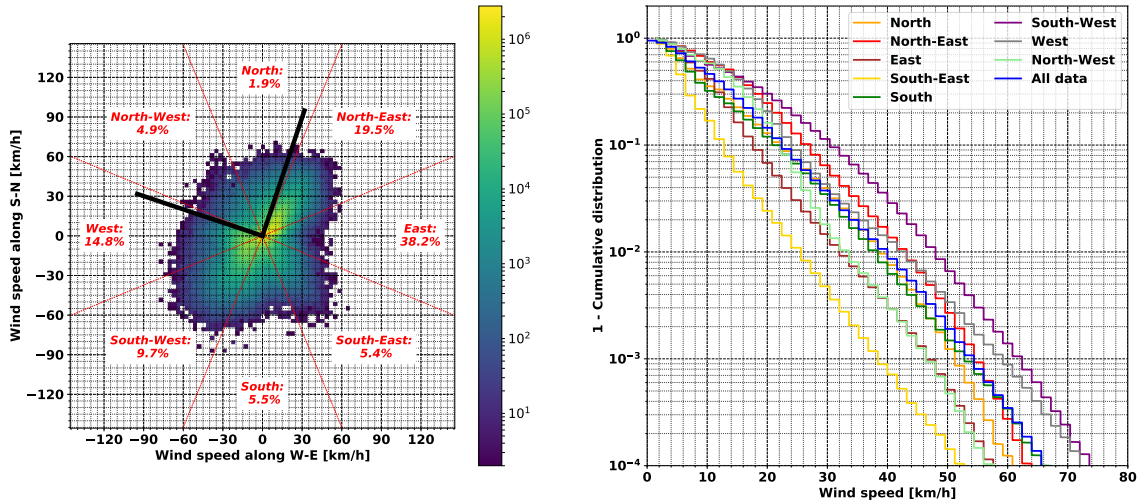


Figure 20: Wind statistics as measured by the EGO weather station during the O3 run. The left plot shows the joint distribution of the wind speed and orientation, with the two black bars showing the directions of the two arms of the Virgo detector. The right plot shows the complementary cumulative distribution of the wind speed for each of the eight quadrants of the wind rose.

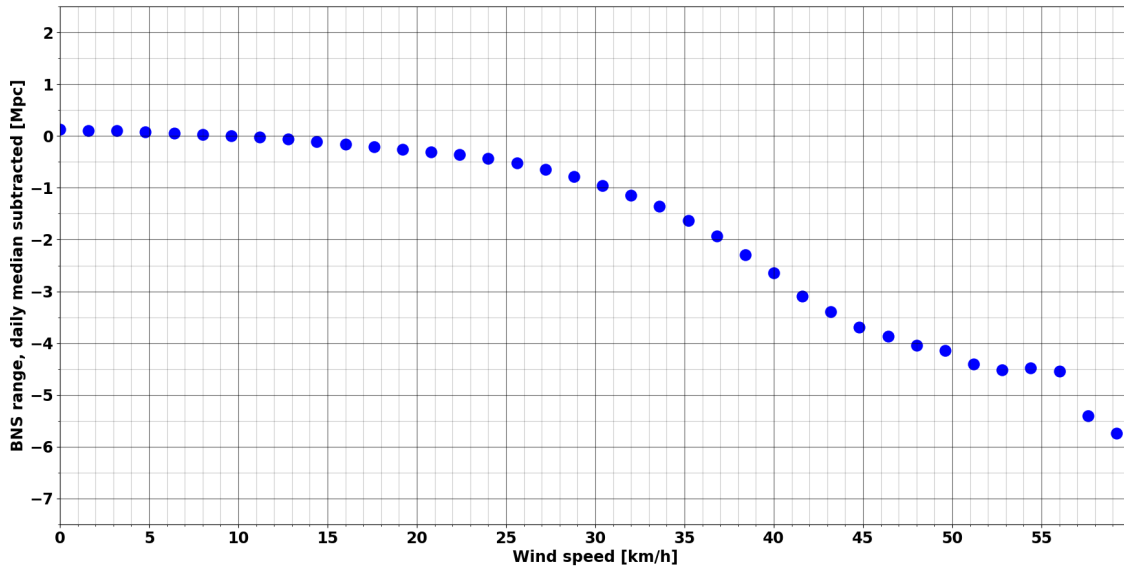


Figure 21: Average variation of the BNS range around its local average, as a function of the wind speed. In the Virgo DAQ, the BNS range and the wind speed are updated every 4 and 2 seconds, respectively.

610 larger these corrections, the more the detector is vulnerable to additional disturbances  
 611 that could make the corrections saturate and lead to an almost immediate control loss.  
 612 The effect of the wind speed is clearly visible on Fig. 22 that compares the

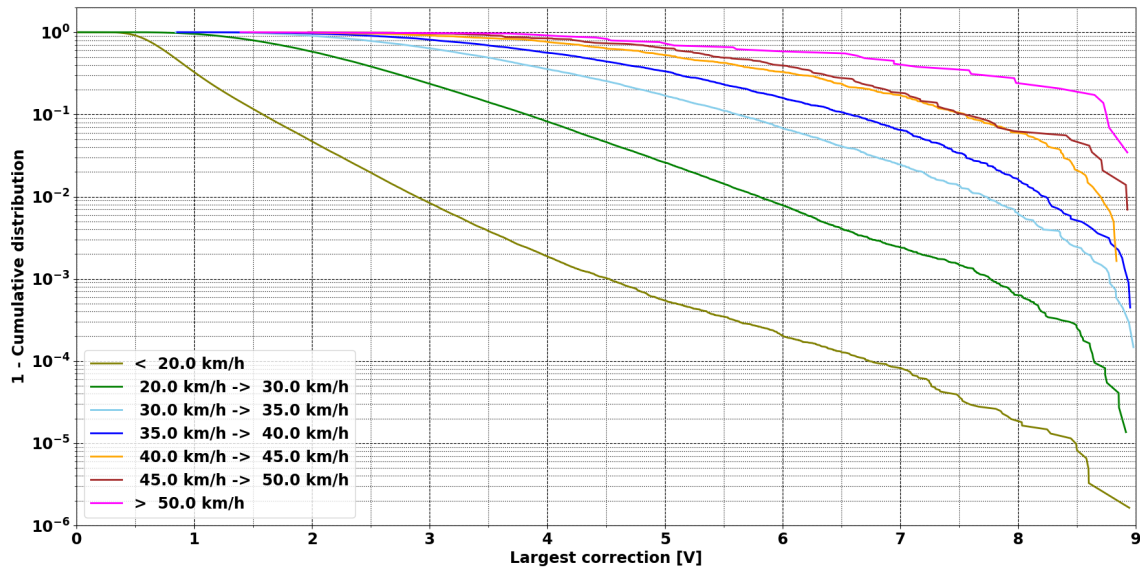


Figure 22: O3 complementary cumulative distribution functions of the maximum longitudinal corrections (in volts) keeping the Virgo arm cavities resonant for different wind speed ranges. The mean wind speed and the maximal corrections have been computed over 30 s time windows. The  $x$ -axis ends at 9 V, a bit below the saturation level of 9.5 V for that particular correction.

613 complementary cumulative distribution functions of the kilometric Fabry-Perot cavity  
 614 longitudinal corrections for different ranges of wind speed. Clearly, the larger the wind  
 615 speed, the higher the correction. On this plot, the average wind speed and the maximum  
 616 correction have been computed using non-overlapping time windows of 30 seconds each.  
 617 The largest displayed correction range stops on purpose at 9 V because the actual  
 618 physical correction saturates at 9.5 V, a value that can be reached or even exceeded  
 619 when there is a control loss. As the control system has some small but non-zero internal  
 620 latency, it is not always clear whether the observed saturation is the cause of the control  
 621 loss or a consequence of it. Therefore, for a cumulative plot like the one shown on Fig. 22,  
 622 corrections above 9 V have been cut away to avoid contamination from correction signals  
 623 posterior to control losses.

### 624 5.3. Disentangling sea activity and wind

625 Fig. 23 attempts to disentangle the impact of high microseism levels (due to the nearby  
 626 rough sea) and high wind, by looking at the O3 Virgo duty cycle as a function of  
 627 the microseism level for three different wind conditions: no cut on wind speed (blue  
 628 histogram); low wind speed (below 25 km/h, green); high wind speed (above 25 km/h,  
 629 red). One can see that in low wind conditions the duty cycle is pretty much independent  
 630 from microseismicity whereas it is lower and decreases more quickly when microseism

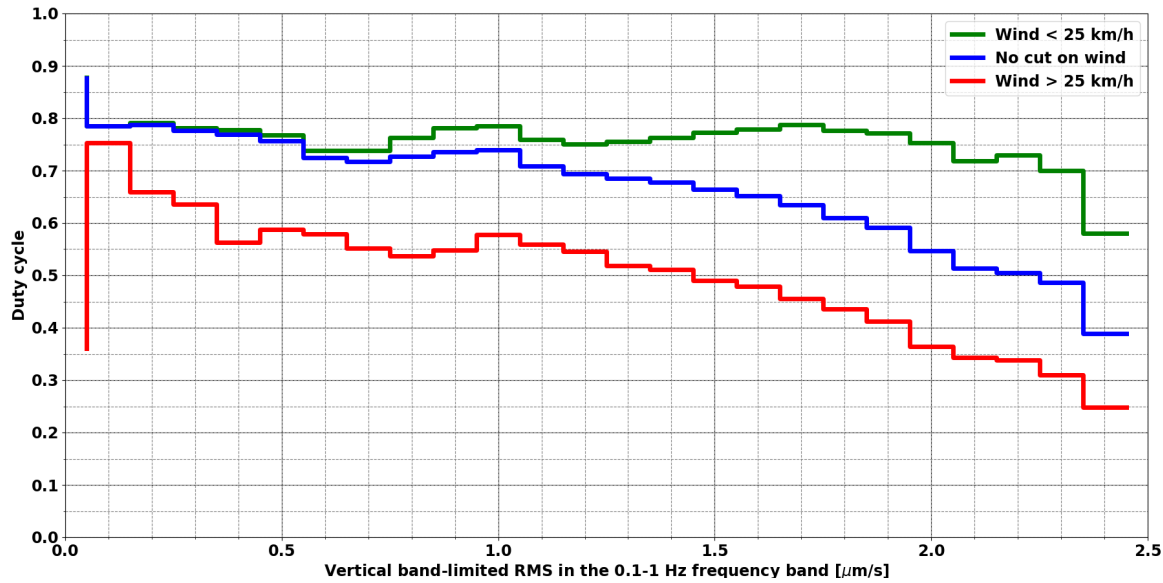


Figure 23: Virgo duty cycle during the O3 run versus microseism activity, for three different wind conditions: blue  $\leftrightarrow$  no cut on wind speed; green  $\leftrightarrow$  low wind (speed below 25 km/h); red  $\leftrightarrow$  high wind (speed above 25 km/h).

631 levels increase. Therefore, the Virgo detector appears robust against microseism but  
 632 more sensitive to wind. Note that the extreme bins on the histograms plotted on  
 633 Fig. 23 may have low statistics compared to others (low wind and high microseism,  
 634 or high wind and low microseism are rare conditions): this explains why the duty cycles  
 635 reported there fluctuate significantly compared to neighboring bins.

## 636 6. Other environment impacts

637 Additional sources of external noise have potential impact on the interferometer.  
 638 Hereafter we describe those sources that we have further investigated during O3, namely:  
 639 Schumann’s resonance magnetic fields, lightning strikes and cosmic ray muons.

### 640 6.1. Magnetic noise

641 Ambient magnetic fields can couple to GW interferometers, for example through the  
 642 magnetic actuators used for the control of the seismic isolation platforms of optical  
 643 components and of the test masses [11, 47]. Like gravitational waves, electromagnetic  
 644 (EM) waves travel at the speed of light, and, due to their strength, could affect multiple  
 645 detectors with time differences compatible with those expected from some GW.

646 Magnetic fields that extend over the entire planet, such as the Schumann resonances [48]  
 647 (SR), or large-current lightning strikes, can limit the sensitivity to GW signals correlated

648 over multiple detectors [49, 50]. One purpose of the EGO external magnetometers (see  
649 Sec. 2) is to monitor the level of these global magnetic fields.

650 At Virgo, the external magnetic environment is much quieter than inside experimental  
651 halls where stray magnetic fields are radiated by electric loads and cables where large  
652 currents are circulating. Figure 24 compares inside and outside magnetometer spectra  
653 recorded at Virgo during O3 and in the very quiet environment inside the Sos Enattos  
654 mine in Sardinia [51]. The most intense spectral noise features are narrow lines at the  
655 50 Hz electric mains frequency and its odd harmonics. The RMS amplitude of the 50 Hz  
656 line measured at Virgo is of the order of 0.1 nT in the external location, while it is at  
657 least 50 times larger in any inside location.

658 Virgo external magnetometers detect the SR field. This consist of steady EM waves  
659 that resonate inside the waveguide formed by the Earth surface and the ionosphere, and  
660 which are excited by globe-wide lightning activity. The second and third SR modes  
661 (peak frequency around 14 Hz and 21 Hz, respectively) are visible above noise at almost  
662 any time, their median amplitude during O3 is a few tenth of pT, their intensity follows  
663 a 24-hour modulation. The measured daily modulation of the third SR mode is shown  
664 in Fig. 25. This modulation is thought to be associated to temperature-driven variations  
665 in the height of the ionosphere EM waveguide [52]. The first SR mode and those of order  
666 greater than three, are often covered by anthropogenic magnetic noise. Figure 25 shows  
667 that during the COVID-19 lockdown period from March to May 2020, the external  
668 magnetic field median RMS in the low frequency region from 1 to 6 Hz reduced by  
669 about 50% with respect to the reference period between December 2019 and February  
670 2020. At the same time, the magnetic field RMS amplitude between 18 Hz and 24 Hz  
671 around the 3<sup>rd</sup> Schumann mode, did not change appreciably.

672 At EGO, anthropogenic external magnetic noise follows a daily modulation: broad  
673 maxima during working hours and minima around 01:00 LT. This noise has the form  
674 of short transients with intensity of  $\approx 10$  pT extending from DC up to approximately  
675 20 Hz. We believe this noise is associated to train transits along railway tracks at about  
676 6 km distance from the site. The sudden trunk-line change when a train passes from an  
677 electro-duct section to another one creates stray currents and magnetic fields that are  
678 observed as magnetic glitches at EGOe. According to the measured coupling of ambient  
679 fields [11] we estimate a negligible impact of Schumann's and anthropogenic magnetic  
680 noise on the sensitivity of the future Virgo upgrades. More relevant might be the impact  
681 of the correlated Schumann noise on multiple interferometers, which is under evaluation.

## 682 6.2. Lightnings

683 Lightning strikes produce prompt EM waves and much slower air pressure waves which  
684 induce vibrations of the ground and of the detector mechanical components. There are  
685 studies of correlated lightnings noise between the Virgo and LIGO sites [50] and at the  
686 KAGRA underground observatory [53].



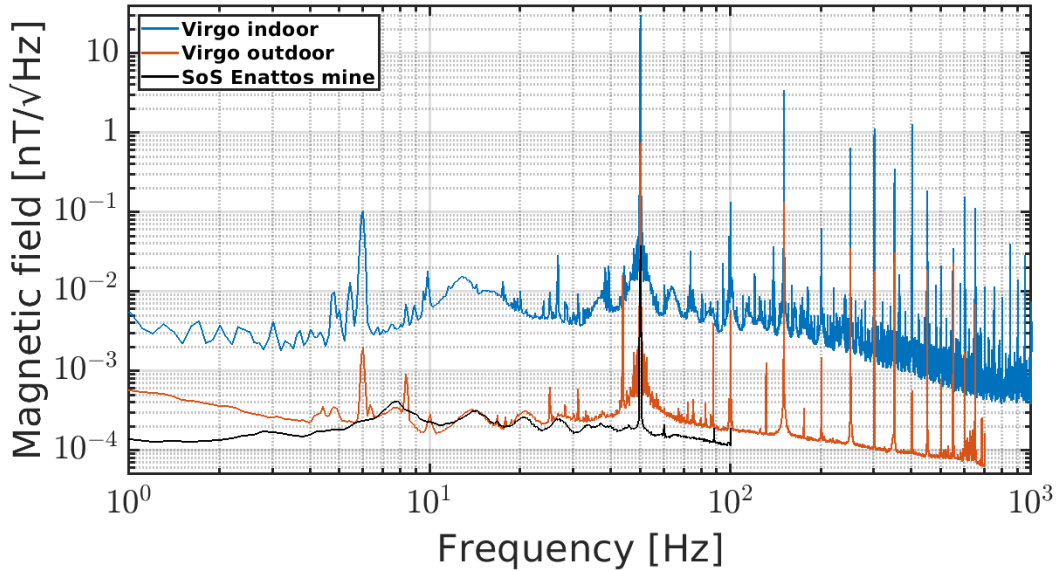


Figure 24: Amplitude spectral densities of indoor (blue curve) and outdoor (red curve) magnetometers at EGO and at Sos Enattos mine in Sardinia (black curve). The quiet Sos Enattos location shows evidence of Schumann resonances peaked at approximately 8, 14, 21, 27 and 33 Hz.

687 The typical effect of the impact of a lightning strike occurring at approximately 10  
 688 kilometers from the Virgo detector during O3 is illustrated in Fig. 26. A distinctive  
 689 feature of lightning strikes is a coincident short transient noise in magnetometers located  
 690 inside the 3 km-distant Virgo experimental buildings (top graph of Fig. 26). The  
 691 magnetic impulse is followed by the slower sound shock wave detected by seismometers  
 692 (middle graph of Fig. 26). The bulk of displacement noise reaching the buildings is  
 693 below 10 Hz.

694 The bottom graph of Fig. 26 illustrates the effect of the lightning in the GW strain signal.  
 695 In coincidence with the spike in magnetometers, we observe a prompt broadband low-  
 696 frequency noise and the onset of a 48 Hz narrow spectral noise, with a minute-long decay  
 697 time, leading to a  $\sim 30\%$  drop of the live BNS range. This latter noise has been associated  
 698 to one structural mode of the West end test mass suspension, which gets excited because  
 699 of the coupling of ambient magnetic fields with the magnetic actuators located along  
 700 the suspension. Moreover, associated with the delayed acoustic and seismic bursts of  
 701 ambient noise reaching the experimental buildings, a broadband strain noise shows up,  
 702 extending up to about 100 Hz. This is likely due to scattered light processes within the  
 703 interferometer.

704 Data quality flags triggered by lightning strikes were produced during the O3 run; they  
 705 proved useful in a test aiming at filtering out part of the false-alarm triggers found by  
 706 a real-time transient GW search [18]. Further studies are planned during the O4 run  
 707 preparation.

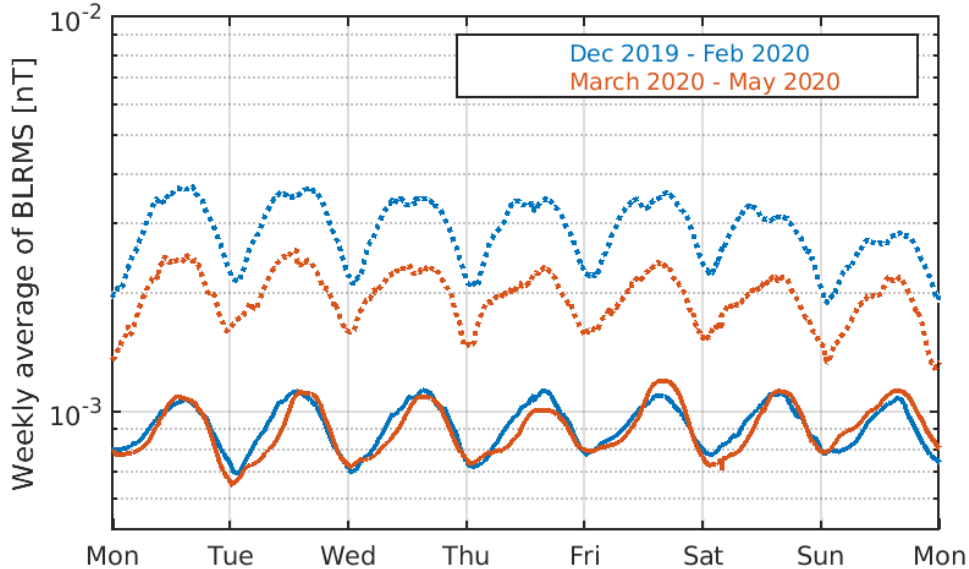


Figure 25: Weekly averaged magnetic field band-limited RMS value computed in two frequency bands: 1 to 6 Hz (dashed) and 18 to 24 Hz (solid). Magnetic field intensity is measured externally of Virgo experimental buildings, in the reference period between December 2019 and February 2020 (blue curves) and in the period between March 15 and May 15 (red curves) which corresponds to reduced anthropogenic activity within and outside of EGO because of the COVID-19 pandemics.

### 708 6.3. Cosmic muons

709 Ground-based GW detectors are constantly passed through by *muons*, produced by  
 710 the interaction of cosmic rays with Earth's atmosphere [54]. This energetic charged  
 711 particles can interact with the detector test masses and constitute an additional source  
 712 of noise, as addressed in the literature since the first prototypes of resonant mass GW  
 713 detectors [55, 56, 57, 58].

714 We report here the preliminary results on the first measurement of potential effects of  
 715 these muons on the Virgo detector noise. Further result can be found in [59]. This study  
 716 has been carried out by means of about 17 days, at the end of the O3b run, of joint data  
 717 acquisition of Virgo and a muon telescope designed by the IP2I laboratory [60], installed  
 718 in the CEB close to the beam splitter mirror. Two kind of tests have been performed.  
 719 In the first one, we have evaluated whether the rate of muons in the correspondence of  
 720 GW candidate events was larger than the reference values of the period: we have found  
 721 no statistical evidence of an excess of muons in correspondence of these triggers. In the  
 722 second test, we have estimated the correlation of this rate with the rate of glitches in  
 723 Virgo noise. Figure 27 shows the time series corresponding to the rates of glitches and  
 724 muons, averaged on strides of 30 minutes. Here, a correlation is clearly evident. This

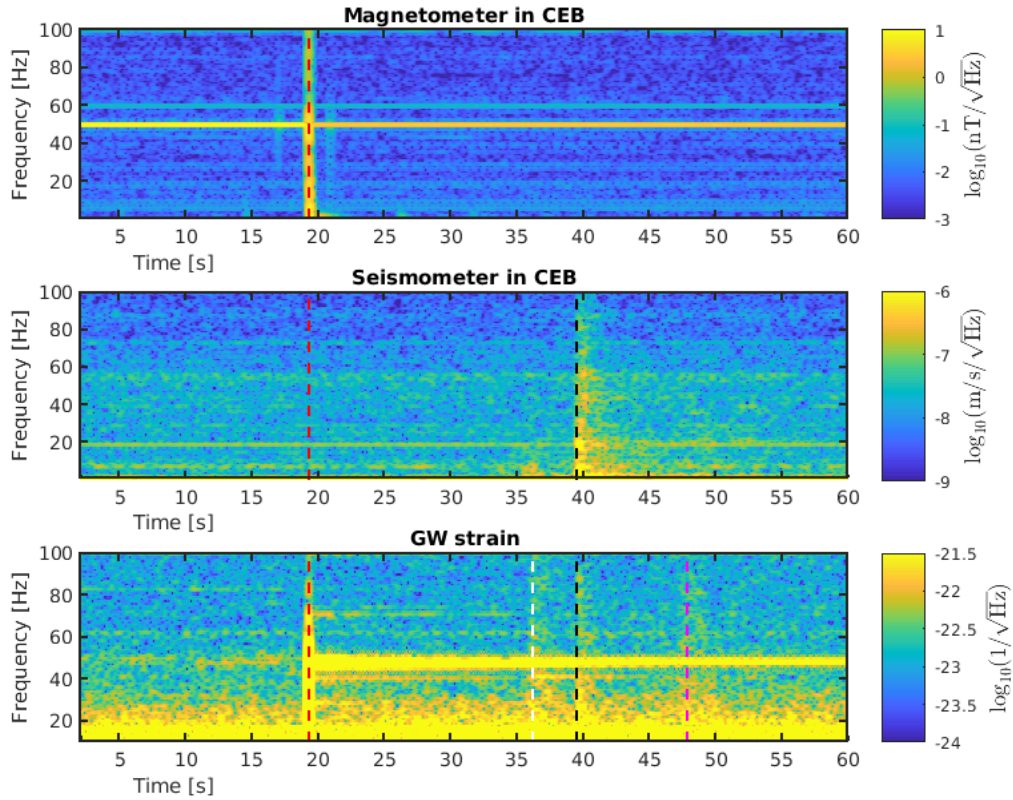


Figure 26: Impact on the Virgo environment and detector of one lightning strike which occurred 6 to 10 km away from Virgo buildings on November 15, 2019 at 23:25:51 UTC. The spectrograms of a few relevant signals are shown. (Top) A prompt magnetic transient is detected by magnetometers at the time of the event, marked by the red vertical line. (Middle) A few seconds later, a seismic (and acoustic, not shown) transient is detected in the central experimental area, marked by the black vertical line. The bottom spectrogram shows the GW strain reconstructed signal during the same time interval. The red vertical line marks the lightning strike occurrence, the black, magenta and white vertical lines mark the occurrence of seismic transients detected in the Central, North and West experimental buildings, respectively.

725 is actually not surprising, for the number of the muons arriving at ground being highly  
 726 dependent on air density and ultimately on parameters like atmospheric pressure and  
 727 temperature. These quantities are also witnesses of the weather conditions, which in  
 728 turn can determine an increase of the detector noise, as we have commented in Sec. 5.1.  
 729 Therefore, both the variations of these rates share the same main cause, which explain  
 730 their large correlation. Once the effects of the atmospheric conditions are removed via  
 731 a regression analysis, the residuals exhibit no significant correlation.

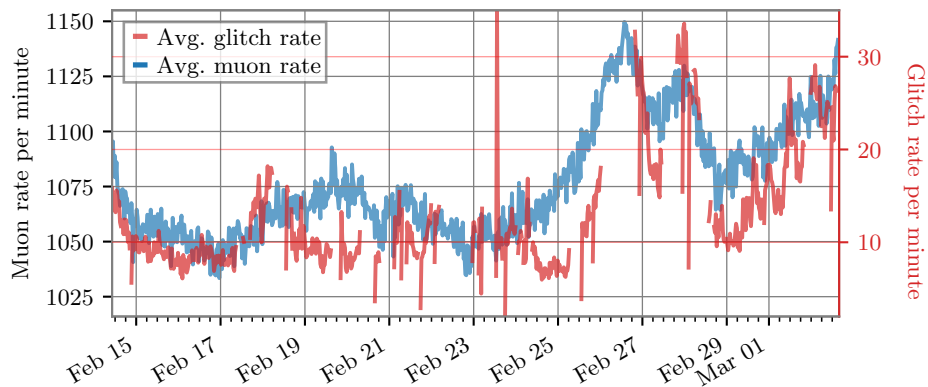


Figure 27: Correlation between muon and glitch rates. The blue line represents the time series of the average rate per minute of muons while the red one is the time series of the rate per minute of glitches with  $\text{SNR} > 4.5$  and frequency at peak in  $[10, 4096]$  Hz as identified by the Omicron pipeline [39]. Gaps in the latter correspond to periods when the detector was not in low noise conditions.

## 732 7. Outlook and prospects for O4

733 The Virgo detector performances are affected by external environment conditions; in  
 734 particular, seismic noise, earthquakes, bad weather, magnetic noise and lightnings have  
 735 an impact on the detector sensitivity or duty cycle. The main coupling mechanisms are:  
 736 direct excitation of suspended mirrors, vibration of experimental buildings, shaking of  
 737 benches hosting auxiliary optical systems, disturbances on critical electronic equipment,  
 738 scattered light.

739 If the detector control system is able to manage the effect of a disturbance, the  
 740 interferometer can remain locked with a reduced sensitivity, otherwise it unlocks and  
 741 the procedure to recover the working point has to be started again, thus impacting on  
 742 the duty cycle.

743 In this work we reported the results of the analysis of such events during the run O3.  
 744 Thanks to the large amount of data collected, we were able to perform a careful statistical  
 745 analysis of the impact of several kinds of external disturbances.

746 The results confirm that the Virgo detector is a very robust apparatus. The sensitivity  
 747 reduction due to anthropogenic seismic noise is very low: less than 2% in terms of BNS  
 748 range. Also the degradation due to the wind is limited: it appears only for wind speeds  
 749 larger than 25 km/h, reaching a sensitivity reduction as large as 10% only for very high  
 750 speed (larger than 50 km/h).

751 In these cases, the sensitivity reduction is due to an increased noise at low frequency as  
 752 well as to the appearance of short high frequency glitches. In few cases, such kind of  
 753 noise was indirectly originated by lightnings.

754 Both microseism and wind have an impact on the detector duty cycle, since the  
755 increasing correction signals acting on the mirror during bad weather can saturate,  
756 finally resulting to an unlock. It results that the Virgo detector global control is more  
757 robust against microseism while it is less effective against strong wind.

758 The analysis of lock losses during O3 confirms that earthquakes are a relevant source  
759 of unlock. The Seismon framework, useful to keep the detector in a safe state to avoid  
760 unlocking during such events, was used during the whole O3 run and it is now being  
761 upgraded for the next scientific run.

762 An upgrade of the environmental monitoring system is in progress to better face the  
763 influence of external disturbances: installation of a new lightning detector in the central  
764 area; installation of two additional weather stations at the end buildings to monitor local  
765 wind gusts; and the installation of more sensitive accelerometers on locations prone to  
766 light scattering (viewports, external optical benches, etc.).

767 These actions, together with several other upgrades of the Virgo detector, already  
768 performed or presently in progress, will have a crucial role for the success of the next  
769 scientific run O4, which is expected to start in the second half of 2022.

## 770 Acknowledgements

771 **October 2020 version** – <https://tds.virgo-gw.eu/q1/?c=15940>

772 The authors gratefully acknowledge the Italian Istituto Nazionale di Fisica Nucleare  
773 (INFN), the French Centre National de la Recherche Scientifique (CNRS) and the  
774 Netherlands Organization for Scientific Research, for the construction and operation  
775 of the Virgo detector and the creation and support of the EGO consortium. The  
776 authors also gratefully acknowledge research support from these agencies as well as by  
777 the Spanish Agencia Estatal de Investigación, the Consellera d’Innovació, Universitats,  
778 Ciència i Societat Digital de la Generalitat Valenciana and the CERCA Programme  
779 Generalitat de Catalunya, Spain, the National Science Centre of Poland and the  
780 Foundation for Polish Science (FNP), the European Commission, the Hungarian  
781 Scientific Research Fund (OTKA), the French Lyon Institute of Origins (LIO),  
782 the Belgian Fonds de la Recherche Scientifique (FRS-FNRS), Actions de Recherche  
783 Concertées (ARC) and Fonds Wetenschappelijk Onderzoek – Vlaanderen (FWO),  
784 Belgium. The authors gratefully acknowledge the support of the NSF, STFC, INFN,  
785 CNRS and Nikhef for provision of computational resources.

786 *We would like to thank all of the essential workers who put their health at risk during*  
787 *the COVID-19 pandemic, without whom we would not have been able to complete this*  
788 *work.*

## 789 Appendix A. Study of the lock losses during O3

790 The Virgo detector needs to be controlled accurately in order to be sensitive to  
 791 gravitational-wave signals [16, 17]. Schematically, there is an automated procedure [18]  
 792 that brings the instrument from an initial state where the optics and the laser are  
 793 controlled independently one from another, to the nominal state where the different  
 794 optical cavities are jointly resonant and the interferometer itself is used as a length  
 795 etalon to control further the laser frequency. That procedure typically takes about  
 796 15-20 minutes and requires 1-2 attempts to complete. Then, the global control of the  
 797 detector is kept as long as possible, with feedback loops maintaining Virgo at its nominal  
 798 working point. When that control is lost for whatever reason, data taking stops and  
 799 the control acquisition procedure has to be started again. This leads to a decrease of  
 800 the instrument duty cycle and can cause transient gravitational waves to be missed.  
 801 Therefore, it is important to find out the causes of the control losses and to use this  
 802 information to improve the feedback systems and make them more robust.

803 As explained in Sec. 4 above, a global study of the control losses was needed to be  
 804 able to extract those likely due to earthquakes. It was decided to focus on the 601  
 805 control losses that occurred during O3 while the detector was taking data in nominal  
 806 conditions (Science mode), to be sure that no particular human action was happening  
 807 on the instrument at any of these times. Related to the duration of the O3 run (about  
 808 11 months) and to the duty cycle of the Virgo detector (about 75%), this corresponds  
 809 to about 1 control loss every 10 hours of data taking on average. And, in reality,  
 810 uninterrupted data taking stretches could be much longer as control losses usually cluster  
 811 in time when a particular problem impacts the detector.

812 The first part of the study was to define the time the control loss occurred for each of  
 813 these events. For that we have used three different Virgo DAQ channels.

- 814 • Two fast channels, sampled at 10 kHz: `ARM_POWER`, latching when the power stored  
 815 in the kilometric arm cavities goes below some threshold, meaning that they are  
 816 not resonant anymore; `DARK_FRINGE_SHUTTER`, triggered when the fast shutter  
 817 protecting the dark fringe photodiodes from an excess of light [2] closes.
- 818 • One slow channel, sampled at 1 Hz: `AUTOMATION_STATUS`, monitoring the global  
 819 status of the detector, as seen by the automation process that steers the instrument.

820 The time of a control loss is defined as the earliest time one of these three switches flips  
 821 from its nominal value to the value corresponding to an uncontrolled detector. Most of  
 822 the time, as expected, the fast channels are the first ones to latch. And they do almost  
 823 simultaneously, given that the cavity resonance losses are all connected. Though, in  
 824 practice, the dark fringe shutter closes almost always before the cavity arm power has  
 825 decreased below its nominal threshold. In addition there are a few cases for which the  
 826 central automation system triggers first a shutdown of the detector global control, either  
 827 because it has detected an issue or because it has received a manual abort request from

ARM_POWER	DARK_FRINGE_SHUTTER	AUTOMATION_STATUS	Total
14	559	28	601

Table A1: Number of control losses witnessed first by each DAQ channel used to time accurately control losses. As expected, the two fast channels are by far those that detect a control loss first. Most of the time the fast shutter protecting the dark fringe photodiodes closes before the arm power loss gets large enough to trigger the other fast channel.

Error	Manual	Hardware	Control software	PI	Earthquakes	Total
2	10	92	7	2	30	143 (24%)

Table A2: Sure causes for 143 O3 control losses – see text for details.

828 the operator on duty. Table A1 shows the breakout of witnesses for the O3 control losses  
829 that occurred while taking Science data.

830 Then, the selected strategy consists in testing several hypothesis in parallel for each  
831 of these events – the main hypothesis investigated are listed in Tabs. A2 and A3 and  
832 documented in the neighbouring text.

833 Various algorithms scanning the data around the control loss have thus been developed,  
834 with the twofold goals of being

- 835 • *complete*: to have as many control losses as possible tagged by at least one control  
836 loss hypothesis;
- 837 • *selective*: to find the right control loss origin as often as possible.

838 Achieving (close to) completeness requires testing many hypothesis, while a profusion  
839 of algorithms could be detrimental to the selectivity of the method. Therefore, the  
840 classification starts with a subset of hypothesis, those that, when identified, certainly  
841 cause a control loss and are also very likely to be the root cause of that particular  
842 event. Obvious examples in that category – called *sure* in the following – are control  
843 losses induced manually by the operator on duty, or hardware problems unambiguously  
844 identified by the real-time monitoring system of the Virgo detector. These control  
845 loss hypothesis are independent by definition and the associated algorithms should be  
846 selective. This has been checked by processing the 601 O3 control losses studied. All  
847 these events have been associated with at most one control loss hypothesis belonging to  
848 the sure category: 24% with one, 76% with none.

849 Table A2 provides details about the 143 control losses whose cause has been tagged as  
850 sure, as described above. The dominant class is hardware problems, mainly transient  
851 interruptions of the data flow coming from some suspensions and causing feedback  
852 control systems to fail. The faulty components have been identified and replaced during

Fast unlocks	Actuation saturation	DARM control inaccuracy	Power loss in sidebands	Arm power asymmetry	Likely missing data	Automation decision	Others	Total
173	85	77	22	4	10	23	64 (11%)	458 (76%)

Table A3: Breakout of control losses by category. 64 (about 11% of the total number of control losses recorded in Science mode during the O3 Virgo run) control losses have not been accurately classified, either because none of the tested hypothesis seemed to match the recorded data or because too many hypothesis were found matching, making their classification inconclusive. Further studies will be done when pre-O4 control losses data become available, in order to make the current classification more complete.

853 the post-O3 shutdown and upgrade phase. Therefore, these problems are not expected  
854 to reoccur during the O4 run. Then, earthquakes are the second most common source  
855 of control losses in the sure category; about three times a month on average. Manual  
856 control losses induced by the operator on shift follow: they are due to the need to switch  
857 from nominal data taking to another task: weekly maintenance, regular calibration or  
858 commissioning activity. In O4 and beyond, such control losses should no longer occur as  
859 the procedure will be updated to require leaving Science mode before manually aborting  
860 the control. In 7 cases (only 1% of the total control losses) the source of the event could  
861 be traced to some software problem; 2 more cases were due to human errors.

862 Finally, two control losses are labelled as *PI* for parametric instabilities, an  
863 optomechanical phenomenon due to the interaction between optical and mechanical  
864 modes of the detector and that had been observed at LIGO in 2015 before finally  
865 being seen in Virgo as well in January 2020 [61]. If not mitigated, a PI can make  
866 control systems saturate in a deterministic way (meaning that the saturation will  
867 consistently reoccur as long as the detector remains in a configuration favourable for  
868 its appearance and growth), thus impacting the detector duty cycle. Moreover, it is  
869 impossible to predict exactly what combinations of the instrument parameters will lead  
870 to a PI. Therefore, a dedicated simulation framework has been developed to estimate  
871 the susceptibility of Virgo to PIs during O3, for O4, and beyond [62].

872 Table A3 describes how the remaining control losses ( $\sim 76\%$ ) have been classified. 11%  
873 of the total remain unclassified, either because none of the hypothesis tested matched, or  
874 because too many did and there was no clear way to find out which one was the root cause  
875 (if identified). The largest category by far (29%) are the so-called *fast unlocks*, events  
876 that are almost instantaneous and occur within the laser injection system, upstream of  
877 the interferometer. Such control losses have been present for years, at rates that strongly  
878 vary over time, ranging from crisis periods lasting some hours to very quiet times. Their  
879 origin is not understood yet and dedicated studies are ongoing to understand the fast  
880 unlock mechanism(s) and find ways to cure or at least mitigate that phenomenon. The



881 next five categories are all related to the variety of feedback control systems that are  
 882 running in parallel to keep the whole detector at its nominal working point. Improving  
 883 the accuracy and the robustness of these systems while making the instrument more  
 884 complex and thus more sensitive to the passing of gravitational wave is a permanent  
 885 challenge, taken up during each upgrade or commissioning phase.

886 The analysis of the O3 control losses has been made using two independent software  
 887 frameworks whose results have been compared: they have been found in good agreement,  
 888 in particular for the dominant control loss categories. With the experience gained during  
 889 O3, the goals for O4 are to improve the monitoring of the control losses and to reduce  
 890 the latency of their analysis. A software framework similar to the Data Quality Reports  
 891 (DQR) [18, 63, 64] used to vet in real time the gravitational-wave transient candidates  
 892 that are significant enough to trigger a public alert is under development. In this  
 893 analogy, the DQR signal candidates are replaced by the control losses and the set of  
 894 checks ran in parallel to assess the quality of the data around a candidate becomes  
 895 the various hypothesis that are tested for each control loss. This improved tool should  
 896 be available in the coming months, during the commissioning phase of the new double-  
 897 recycled Advanced Virgo detector and the associated noise hunting activities to improve  
 898 the overall sensitivity of the instrument.

## 899 References

- 900 [1] Aasi J *et al.* (LIGO Scientific) 2015 *Class. Quant. Grav.* **32** 074001 (*Preprint* 1411.4547)  
 901 [2] Acernese F *et al.* (Virgo Collaboration) 2015 *Class. Quant. Grav.* **32** 024001 (*Preprint* 1408.3978)  
 902 [3] Akutsu T *et al.* 2021 *Progress of Theoretical and Experimental Physics* **2021** ISSN 2050-  
 903 3911 05A102 (*Preprint* [https://academic.oup.com/ptep/article-pdf/2021/5/05A102/](https://academic.oup.com/ptep/article-pdf/2021/5/05A102/38109702/ptab018.pdf)  
 904 [38109702/ptab018.pdf](https://academic.oup.com/ptep/article-pdf/2021/5/05A102/38109702/ptab018.pdf)) URL <https://doi.org/10.1093/ptep/ptab018>  
 905 [4] Abbott B *et al.* (LIGO Scientific Collaboration, Virgo Collaboration) 2016 *Phys. Rev. Lett.* **116**  
 906 061102 (*Preprint* 1602.03837)  
 907 [5] Abbott B *et al.* (LIGO Scientific Collaboration, Virgo Collaboration) 2017 *Phys. Rev. Lett.* **119**  
 908 161101 (*Preprint* 1710.05832)  
 909 [6] Abbott B *et al.* (LIGO Scientific Collaboration, Virgo Collaboration, Fermi GBM, INTEGRAL,  
 910 IceCube Collaboration, AstroSat Cadmium Zinc Telluride Imager Team, IPN Collaboration,  
 911 Insight-HXMT Collaboration, ANTARES Collaboration, Swift Collaboration, AGILE Team,  
 912 1M2H Team, Dark Energy Camera GW-EM Collaboration, DES Collaboration, DLT40,  
 913 GRAWITA, Fermi-LAT Collaboration, ATCA, ASKAP, Las Cumbres Observatory Group,  
 914 OzGrav, DWF (Deeper Wider Faster Program), AST3 and CAASTRO Collaborations,  
 915 VINROUGE Collaboration, MASTER Collaboration, J-GEM, GROWTH, JAGWAR,  
 916 CaltechNRAO, TTU-NRAO and NuSTAR Collaborations, Pan-STARRS, MAXI Team,  
 917 TZAC Consortium, KU Collaboration, Nordic Optical Telescope, ePESSTO, GROND, Texas  
 918 Tech University, SALT Group, TOROS Collaboration, BOOTES Collaboration, MWA,  
 919 CALET Collaboration, IKI-GW Follow-up Collaboration, H.E.S.S. Collaboration, LOFAR  
 920 Collaboration, LWA, HAWC Collaboration, Pierre Auger Collaboration, ALMA Collaboration,  
 921 Euro VLBI Team, Pi of Sky Collaboration, Chandra Team at McGill University, DFN,  
 922 ATLAS Telescopes, High Time Resolution Universe Survey, RIMAS, RATIR, SKA South  
 923 Africa/MeerKAT) 2017 *Astrophys. J. Lett.* **848** L12 (*Preprint* 1710.05833)

- 924 [7] Abbott B *et al.* (LIGO Scientific Collaboration, Virgo Collaboration) 2019 *Phys. Rev. X* **9** 031040  
925 (*Preprint* 1811.12907)
- 926 [8] Abbott R *et al.* (LIGO Scientific Collaboration, Virgo Collaboration) 2021 *Phys. Rev. X* **11** 021053  
927 (*Preprint* 2010.14527)
- 928 [9] Abbott R *et al.* 2021 *The Astrophysical Journal Letters* **913** L7 URL [https://doi.org/10.3847/  
929 2041-8213/abe949](https://doi.org/10.3847/2041-8213/abe949)
- 930 [10] Abbott R *et al.* (LIGO Scientific Collaboration and Virgo Collaboration) 2021 *Phys. Rev. D*  
931 **103**(12) 122002 URL <https://link.aps.org/doi/10.1103/PhysRevD.103.122002>
- 932 [11] Fiori I *et al.* 2020 *Galaxies* **8** ISSN 2075-4434 URL <https://www.mdpi.com/2075-4434/8/4/82>
- 933 [12] Nguyen P *et al.* 2021 *Classical and Quantum Gravity* URL [http://iopscience.iop.org/  
934 article/10.1088/1361-6382/ac011a](http://iopscience.iop.org/article/10.1088/1361-6382/ac011a)
- 935 [13] Washimi T *et al.* 2021 *Classical and Quantum Gravity* **38** 125005 URL [https://doi.org/10.  
936 1088/1361-6382/abf89a](https://doi.org/10.1088/1361-6382/abf89a)
- 937 [14] Punturo M *et al.* 2010 *Classical and Quantum Gravity* **27** 194002 URL [https://doi.org/10.  
938 1088/0264-9381/27/19/194002](https://doi.org/10.1088/0264-9381/27/19/194002)
- 939 [15] Acernese F *et al.* 2004 *Astroparticle Physics* **20** 629–640 ISSN 0927-6505 URL [https://www.  
940 sciencedirect.com/science/article/pii/S0927650503002603](https://www.sciencedirect.com/science/article/pii/S0927650503002603)
- 941 [16] Acernese F *et al.* 2020 *Astroparticle Physics* **116** 102386 ISSN 0927-6505 URL [https://www.  
942 sciencedirect.com/science/article/pii/S0927650519301835](https://www.sciencedirect.com/science/article/pii/S0927650519301835)
- 943 [17] Allocca A *et al.* 2020 *Galaxies* **8** ISSN 2075-4434 URL <https://www.mdpi.com/2075-4434/8/4/85>
- 944 [18] The Virgo Collaboration 2021 *In preparation*
- 945 [19] Barone F, De Rosa R, Eleuteri A, Milano L and Qipiani K 2002 *IEEE Transactions on Nuclear  
946 Science* **49** 405–410
- 947 [20] RADIO WAVES below 22 kHz URL <http://www.vlf.it/>
- 948 [21] The OpenStreetMap contributors OpenStreetMap URL <https://www.openstreetmap.org>
- 949 [22] Koley S *et al.* 2017 *SEG Technical Program Expanded Abstracts* 2946–2950 URL [https://doi.  
950 org/10.1190/segam2017-17681951.1](https://doi.org/10.1190/segam2017-17681951.1)
- 951 [23] Longuet-Higgins M S 1950 *Philosophical Transactions of the Royal Society of London. Series A,  
952 Mathematical and Physical Sciences* **243** 1–35
- 953 [24] Cessaro R K 1994 *Bulletin of the Seismological Society of America* **84** 142–148
- 954 [25] Peterson J R 1993 *Open-File Report* URL <http://pubs.er.usgs.gov/publication/ofr93322>
- 955 [26] Flaminio R 2020 Status and plans of the Virgo gravitational wave detector *Ground-based and  
956 Airborne Telescopes VIII* vol 11445 ed Marshall H K, Spyromilio J and Usuda T International  
957 Society for Optics and Photonics (SPIE) pp 205 – 214 URL [https://doi.org/10.1117/12.  
958 2565418](https://doi.org/10.1117/12.2565418)
- 959 [27] Coughlin M *et al.* 2017 *Classical and Quantum Gravity* **34** 044004 URL [https://doi.org/10.  
960 1088/1361-6382/aa5a60](https://doi.org/10.1088/1361-6382/aa5a60)
- 961 [28] Biscans S *et al.* 2018 *Classical and Quantum Gravity* **35** 055004 URL [https://doi.org/10.1088/  
962 1361-6382/aaa4aa](https://doi.org/10.1088/1361-6382/aaa4aa)
- 963 [29] Mukund N *et al.* 2019 *Classical and Quantum Gravity* **36** 085005 URL [https://doi.org/10.  
964 1088/1361-6382/ab0d2c](https://doi.org/10.1088/1361-6382/ab0d2c)
- 965 [30] Product distribution layer git repository URL <https://github.com/usgs/pdl>
- 966 [31] Berni F *et al.* 2012 The Detector Monitoring System <https://tds.virgo-gw.eu/ql/?c=9005>
- 967 [32] F Berni 2020 DMS help manual <https://tds.virgo-gw.eu/ql/?c=15469>
- 968 [33] 2020 Virgo logbook entry validating the use of the eq mode control configuration to take science-  
969 quality data URL <https://logbook.virgo-gw.eu/virgo/?r=48612>
- 970 [34] 2020 Query to the public ingv website URL [http://webservices.ingv.it/fdsnws/event/  
971 1/query?starttime=2019-04-01T15%3A00%3A00&endtime=2020-03-27T17%3A00%3A00&  
972 minmag=2&maxmag=10&mindepth=-10&maxdepth=1000&minlat=27.0&maxlat=48.0&minlon=  
973 -7.0&maxlon=37.5&mininversion=100&orderby=time-asc&timezone=UTC&format=text&  
974 limit=10000](http://webservices.ingv.it/fdsnws/event/1/query?starttime=2019-04-01T15%3A00%3A00&endtime=2020-03-27T17%3A00%3A00&minmag=2&maxmag=10&mindepth=-10&maxdepth=1000&minlat=27.0&maxlat=48.0&minlon=-7.0&maxlon=37.5&mininversion=100&orderby=time-asc&timezone=UTC&format=text&limit=10000)

- 975 [35] INGV seismic surveillance center public website URL <http://terremoti.ingv.it>
- 976 [36] Bernardi F *et al.* 2015 *Natural Hazards and Earth System Sciences* **15** 2019–2036 URL <https://nhess.copernicus.org/articles/15/2019/2015/>
- 977
- 978 [37] Early-est: Earthquake rapid location system with estimation of tsunamigenesis URL <http://early-est.rm.ingv.it/warning.html>
- 979
- 980 [38] Welch P 1967 *IEEE Transactions on audio and electroacoustics* **15** 70–73
- 981 [39] Robinet F *et al.* 2020 *SoftwareX* **12** 100620 ISSN 2352-7110 URL <https://www.sciencedirect.com/science/article/pii/S2352711020303332>
- 982
- 983 [40] Canuel B, Genin E, Vajente G and Marque J 2013 *Opt. Express* **21** 10546–10562 URL <http://www.opticsexpress.org/abstract.cfm?URI=oe-21-9-10546>
- 984
- 985 [41] Waş M, Gouaty R and Bonnard R 2021 *Classical and Quantum Gravity* **38** 075020 URL <https://doi.org/10.1088/1361-6382/abe759>
- 986
- 987 [42] Accadia T *et al.* 2010 *Classical and Quantum Gravity* **27** 194011 URL <https://doi.org/10.1088/0264-9381/27/19/194011>
- 988
- 989 [43] Van Heijningen J V *et al.* 2019 *Class. Quant. Grav.* **36** 7 URL <https://iopscience.iop.org/article/10.1088/1361-6382/ab075e>
- 990
- 991 [44] Valdes G, O'Reilly B and Diaz M 2017 *Class. Quant. Grav.* **34** 235009
- 992 [45] Longo A *et al.* 2020 *Class. Quant. Grav.* **37** 145011 (*Preprint* 2002.10529)
- 993 [46] Li H, Li Z and Mo W 2017 *Signal Processing* **138**
- 994 [47] Cirone A *et al.* 2018 *Rev. Sci.* **89** 114501 URL <https://doi.org/10.1063/1.5045397>
- 995 [48] Schumann W 1952 *Zeitschrift Naturforschung Teil A* **7** 149
- 996 [49] Coughlin M W *et al.* 2018 *Phys. Rev. D* **97**(10) 102007 URL <https://journals.aps.org/prd/abstract/10.1103/PhysRevD.97.102007>
- 997
- 998 [50] Kowalska-Leszczynska I *et al.* 2017 *Classical and Quantum Gravity* **34** 074002 URL <https://doi.org/10.1088/1361-6382/2Faa60eb>
- 999
- 1000 [51] Naticchioni L *et al.* 2020 *Journal of Physics: Conference Series* **1468** 012242 URL <https://doi.org/10.1088/1742-6596/1468/1/012242>
- 1001
- 1002 [52] Sentman, D D 1995 *Schumann Resonances* (CRC Press) chap 11
- 1003 [53] Washimi T *et al.* 2021 *Journal of Instrumentation* **16** P07033 URL <https://doi.org/10.1088/1748-0221/16/07/p07033>
- 1004
- 1005 [54] Maurin D, Melot F and Taillet R 2014 *Astronomy & Astrophysics* **569** A32
- 1006 [55] Beron B L and Hofstadter R 1969 *Phys. Rev. Lett.* **23**(4) 184–186 URL <https://link.aps.org/doi/10.1103/PhysRevLett.23.184>
- 1007
- 1008 [56] Amaldi E and Pizzella G 1986 *Il Nuovo Cimento C* **9** 612–620
- 1009 [57] Giazotto A 1988 *Physics Letters A* **128** 241–244 ISSN 0375-9601
- 1010 [58] Chiang J, Michelson P and Price J 1992 *Nuclear Instruments and Methods in Physics Research Section A: Accelerators, Spectrometers, Detectors and Associated Equipment* **311** 603–612 ISSN 0168-9002
- 1011
- 1012
- 1013 [59] The ENV team 2021 Future publication about muons separate paper about Virgo and cosmic muons
- 1014
- 1015 [60] Lesparre N *et al.* 2012 *Geoscientific Instrumentation, Methods and Data Systems* **1** 33–42 URL <https://gi.copernicus.org/articles/1/33/2012/>
- 1016
- 1017 [61] Puppo, P for the Virgo Collaboration 2021 Parametric Instability Observation in Advanced Virgo second European Physical Society Conference on Gravitation: measuring gravity URL [https://agenda.infn.it/event/26098/contributions/132480/attachments/83185/109525/EPS\\_Online2021\\_PI.pdf](https://agenda.infn.it/event/26098/contributions/132480/attachments/83185/109525/EPS_Online2021_PI.pdf)
- 1018
- 1019
- 1020
- 1021 [62] Cohen D *et al.* 2021 Towards optomechanical parametric instabilities prediction in ground-based gravitational wave detectors (*Preprint* 2102.11070)
- 1022
- 1023 [63] The LIGO Scientific Collaboration and The Virgo Collaboration 2018 Data Quality Report User Documentation <https://docs.ligo.org/detchar/data-quality-report>
- 1024
- 1025 [64] Davis D *et al.* 2021 *Classical and Quantum Gravity* **38** 135014 URL <https://doi.org/10.1088/>

